GRAVITATIONAL LENS MODELS BASED ON SUBMILLIMETER ARRAY[*] IMAGING OF *HERSCHEL*[†]-SELECTED STRONGLY LENSED SUB-MILLIMETER GALAXIES AT $z > 1.5$

R. S. BUSSMANN[1], I. PÉREZ-FOURNON[2,3], S. AMBER[4], J. CALANOG[5], M. A. GURWELL[1], H. DANNERBAUER[6], F. DE BERNARDIS[5], HAI FU[7], A. I. HARRIS[8], M. KRIPS[9], A. LAPI[10], R. MAIOLINO[11,12], A. OMONT[13], D. RIECHERS[14], J. WARDLOW[5], A. J. BAKER[15], M. BIRKINSHAW[16], J. BOCK[17,18], N. BOURNE[19], D. L. CLEMENTS[20], A. COORAY[5,17], G. DE ZOTTI[21], L. DUNNE[22], S. DYE[19], S. EALES[23], D. FARRAH[24], R. GAVAZZI[13], J. GONZÁLEZ NUEVO[25], R. HOPWOOD[20], E. IBAR[26], R. J. IVISON[27,28], N. LAPORTE[2,3], S. MADDOX[22], P. MARTÍNEZ-NAVAJAS[2,3], M. MICHALOWSKI[28], M. NEGRELLO[21], S. J. OLIVER[29], I. G. ROSEBOOM[28,29], DOUGLAS SCOTT[30], S. SERJEANT[4], A. J. SMITH[29], MATTHEW SMITH[23], A. STREBLYANSKA[2,3], E. VALIANTE[30], P. VAN DER WERF[31], A. VERMA[32], J. D. VIEIRA[17], L. WANG[29], AND D. WILNER[1]

[1] Harvard-Smithsonian Center for Astrophysics, 60 Garden Street, Cambridge, MA 02138, USA
[2] Instituto de Astrofísica de Canarias (IAC), E-38200 La Laguna, Tenerife, Spain
[3] Departamento de Astrofísica, Universidad de La Laguna (ULL), E-38205 La Laguna, Tenerife, Spain
[4] Department of Physical Sciences, The Open University, Milton Keynes MK7 6AA, UK
[5] Department of Physics & Astronomy, University of California, Irvine, CA 92697, USA
[6] Laboratoire AIM-Paris-Saclay, CEA/DSM/Irfu-CNRS-Université Paris Diderot, CE-Saclay, pt courrier 131, F-91191 Gif-sur-Yvette, France
[7] Department of Physics and Astronomy, The University of Iowa, 203 Van Allen Hall, Iowa City, IA 52242, USA
[8] Department of Astronomy, University of Maryland, College Park, MD 20742-2421, USA
[9] Institut de RadioAstronomie Millimétrique, 300 Rue de la Piscine, Domaine Universitaire, 38406 Saint Martin d'Hères, France
[10] Department Fisica, Univ. Tor Vergata, Via Ricerca Scientifica 1, 00133 Rome, Italy and SISSA, Via Bonomea 265, 34136 Trieste, Italy
[11] Cavendish Laboratory, University of Cambridge, 19 J.J. Thomson Ave., Cambridge CB3 OHE, UK
[12] Kavli Institute for Cosmology, University of Cambridge, Madingley Road, Cambridge CB3 OHA, UK
[13] Institut d'Astrophysique de Paris, UMR 7095, CNRS, UPMC Univ. Paris 06, 98bis boulevard Arago, F-75014 Paris, France
[14] Department of Astronomy, Space Science Building, Cornell University, Ithaca, NY 14853-6801, USA
[15] Department of Physics and Astronomy, Rutgers, The State University of New Jersey, 136 Frelinghuysen Rd, Piscataway, NJ 08854, USA
[16] HH Wills Physics Laboratory, University of Bristol, Tyndall Avenue, Bristol BS8 1TL, UK
[17] California Institute of Technology, 1200 E. California Blvd., Pasadena, CA 91125, USA
[18] Jet Propulsion Laboratory, 4800 Oak Grove Drive, Pasadena, CA 91109, USA
[19] School of Physics and Astronomy, University of Nottingham, NG7 2RD, UK
[20] Astrophysics Group, Imperial College London, Blackett Laboratory, Prince Consort Road, London SW7 2AZ, UK
[21] INAF-Osservatorio Astronomico di Padova, Vicolo dell'Osservatorio 5, I-35122 Padova, Italy
[22] Department of Physics and Astronomy, University of Canterbury, Private Bag 4800, Christchurch, 8140, New Zealand
[23] School of Physics and Astronomy, Cardiff University, Queens Buildings, The Parade, Cardiff CF24 3AA, UK
[24] Department of Physics, Virginia Tech, Blacksburg, VA 24061, USA
[25] Instituto de Física de Cantabria (CSIC-UC), Av. los Castros s/n, 39005 Santander, Spain
[26] Instituto de Astrofísica. Facultad de Física. Pontificia Universidad Católica de Chile. Casilla 306, Santiago 22, Chile
[27] UK Astronomy Technology Centre, Royal Observatory, Blackford Hill, Edinburgh EH9 3HJ, UK
[28] Institute for Astronomy, University of Edinburgh, Royal Observatory, Blackford Hill, Edinburgh EH9 3HJ, UK
[29] Astronomy Centre, Department of Physics & Astronomy, University of Sussex, Brighton BN1 9QH, UK
[30] Department of Physics & Astronomy, University of British Columbia, 6224 Agricultural Road, Vancouver, BC V6T 1Z1, Canada
[31] Leiden Observatory, P.O. Box 9513, NL-2300 RA Leiden, The Netherlands
[32] Department of Astrophysics, Denys Wilkinson Building, University of Oxford, Keble Road, Oxford OX1 3RH, UK

ABSTRACT

Strong gravitational lenses are now being routinely discovered in wide-field surveys at (sub-)millimeter wavelengths. We present Submillimeter Array (SMA) high-spatial resolution imaging and Gemini-South and Multiple Mirror Telescope optical spectroscopy of strong lens candidates discovered in the two widest extragalactic surveys conducted by the *Herschel Space Observatory*: the Herschel-Astrophysical Terahertz Large Area Survey (H-ATLAS) and the Herschel Multi-tiered Extragalactic Survey (HerMES). From a sample of 30 *Herschel* sources with $S_{500} > 100$ mJy, 21 are strongly lensed (i.e., multiply imaged), 4 are moderately lensed (i.e., singly imaged), and the remainder require additional data to determine their lensing status. We apply a visibility-plane lens modeling technique to the SMA data to recover information about the masses of the lenses as well as the intrinsic (i.e., unlensed) sizes (r_{half}) and far-infrared luminosities (L_{FIR}) of the lensed submillimeter galaxies (SMGs). The sample of lenses comprises primarily isolated massive galaxies, but includes some groups and clusters as well. Several of the lenses are located at $z_{lens} > 0.7$, a redshift regime that is inaccessible to lens searches based on Sloan Digital Sky Survey spectroscopy. The lensed SMGs are amplified by factors that are significantly below statistical model predictions given the $500\,\mu$m flux densities of our sample. We speculate that this may reflect a deficiency in our understanding of the intrinsic sizes and luminosities of the brightest SMGs. The lensed SMGs span nearly one decade in L_{FIR} (median $L_{FIR} = 7.9 \times 10^{12}\,L_\odot$) and two decades in FIR luminosity surface density (median $\Sigma_{FIR} = 6.0 \times 10^{11}\,L_\odot\,\mathrm{kpc}^{-2}$). The strong lenses in this sample and others identified via (sub-)mm surveys will

provide a wealth of information regarding the astrophysics of galaxy formation and evolution over a wide range in redshift.

Key words: galaxies: evolution – galaxies: fundamental parameters – galaxies: halos – galaxies: high-redshift – gravitational lensing: strong

Online-only material: color figures

1. INTRODUCTION

Strong gravitational lensing by massive galaxies provides one of the most striking visual confirmations of Einstein's theory of General Relativity. In the case of galaxy–galaxy lensing, the chance alignment of two galaxies along the line of sight provides information about both the lens and the source that cannot be obtained in any other way. The angular separation of multiple images of a lensed galaxy is typically parameterized in terms of the angular Einstein radius (here, denoted θ_E) and provides an unambiguous measurement of the total mass of the lens (baryonic plus non-baryonic) inside θ_E, as long as the distances to the lens and source are known (Schneider et al. 1992). At the same time, lensing increases the apparent size of the background source and conserves surface brightness in the process. A spatially unresolved measurement of the flux density from a lensed source is therefore a factor of order μ (the magnification factor, defined in detail in Section 3.1) brighter than for an unlensed source, while spatially resolved measurements can provide a factor of $\sim\sqrt{\mu}$ higher resolution (Schneider et al. 1992).

Given the benefits of studying strong lenses, it is no surprise that significant efforts have been devoted to the assembly of large samples of them. The earliest of these efforts focused on surveys in the radio with the Jodrell Bank Very Large Array gravitational lens survey (JVAS; King & Browne 1996) and the Cosmic Lens All-Sky Survey (CLASS; Myers et al. 2003) or on *Hubble Space Telescope* (*HST*) follow-up of known strong lenses as part of the Center for Astrophysics Arizona Space Telescope Lens Survey (CASTLeS; Muñoz et al. 1998). Together these surveys have created a sample of ≈80 strong lenses (Schneider et al. 2006). More recently, surveys based on *HST* Advanced Camera for Surveys (ACS) follow-up of candidates selected from Sloan Digital Sky Survey (SDSS) spectroscopy as part of the Sloan Lens ACS Survey (SLACS; Bolton et al. 2008) and the SDSS Quasar Lens Search (SQLS; Inada et al. 2012), as well as candidates selected from the Canada France Hawaii Telescope Legacy Survey as part of the Strong Lensing in the Legacy Survey (SL2S) project (e.g., Sonnenfeld et al. 2013) have more than doubled this number. More recent upgrades associated with the SDSS-III Baryon Oscillation Spectroscopic Survey (BOSS; Eisenstein et al. 2011) promise to increase the sample size of SDSS-selected lenses by a factor of several (the BOSS Emission-Line Lens Survey, or BELLS; Brownstein et al. 2012). Finally, a new method of finding lenses has come to sudden prominence with the launch of the *Herschel Space Observatory* (*Herschel*; Pilbratt et al. 2010) and the advent of the South Pole Telescope (SPT; Carlstrom et al. 2011) and the Atacama

Cosmology Telescope (Swetz et al. 2011): wide-field surveys at submillimeter (sub-mm) and millimeter (mm) wavelengths.

Surveys at (sub-)mm wavelengths are ideal tools for discovering lenses, in part because the observed-frame (sub-)mm flux density of a dusty galaxy at a given luminosity is approximately independent of redshift for $z > 1$ (Blain & Longair 1993) and in part because the number counts of unlensed submm sources (SMGs) falls off very steeply at high flux densities compared to optically selected galaxies (e.g., Barger et al. 1999; Coppin et al. 2006; Oliver et al. 2010; Clements et al. 2010). Strong lensing events are rare, so the key requirement for identifying them is wide-area coverage. This is now being provided by the Herschel Astrophysical Terahertz Large Area Survey (H-ATLAS; Eales et al. 2010), the Herschel Multi-Tiered Extragalactic Survey (HerMES; Oliver et al. 2012),[33] the SPT (Vieira et al. 2010; Mocanu et al. 2013), and ACT (Marsden et al. 2013). In this paper, we focus on strong lens candidates selected from the two *Herschel* surveys.

Studies based on the H-ATLAS Science Demonstration Phase field (covering 14.4 deg^2) and on HerMES (covering 94.8 deg^2) have found that a simple selection at 500 μm of $S_{500} > 100$ mJy finds lenses with an efficiency of 70%–100% (Negrello et al. 2010; Wardlow et al. 2013). This single selection criterion also yields low-z spiral galaxies (Serjeant & Harrison 2005) and blazars with synchrotron emission spectra in the *Herschel* bands (de Zotti et al. 2005), but these are easily identified and removed using shallow optical imaging (SDSS is sufficient) and shallow radio imaging from the National Radio Astronomy Observatory Very Large Array Sky Survey (NVSS; Condon et al. 1998).

A world-wide, multi-wavelength follow-up effort is now underway to study strong lens candidates from H-ATLAS and HerMES that are selected to have $S_{500} > 100$ mJy. The main goals of this effort are to: (1) confirm that the candidates are indeed strong lenses; (2) use the lenses to study massive galaxy evolution over $0.2 < z < 1.3$; and (3) use the lensed SMGs to learn about the nature of star-formation and galaxy evolution in luminous, dusty galaxies at $z \gtrsim 1.5$.

There are three key steps that must be taken to confirm the lensing hypothesis and study a member of the *Herschel* sample in detail: a redshift measurement for the lens (typically from optical spectroscopy); a distinct redshift for the background source (typically from radio or (sub-)mm wave spectroscopy); and spatially-resolved imaging of the source that is consistent with strong lensing. In this paper, we present data that mark significant progress on two of these three fronts. First, we give results from a large, multi-semester program with the Submillimeter Array (SMA; Ho et al. 2004) that comprises over 160 hr of on-source integration time and provides sub-arcsecond, spatially-resolved 880 μm images of 30 *Herschel* lens candidates (some of the SMA data have been published previously and are known lenses—we highlight where this is the case and provide references in Section 3.2). Second, we provide

---

[33] http://hermes.sussex.ac.uk

redshifts from optical spectroscopy of 8 lens candidates obtained with the Multiple Mirror Telescope (MMT), Gemini-South telescope (Gemini-S), William Herschel Telescope (WHT), and Very Large Telescope (VLT). Redshift measurements for the background sources for nearly all of the objects in this paper are already available from a wide range of facilities (see Section 2.1).

We use the SMA imaging, optical spectroscopy, and radio or (sub-)mm wave spectroscopy to determine which of the *Herschel*-selected lens candidates are indeed strongly lensed ($\mu > 2$, with multiple images of the lensed source), which are only moderately lensed ($1 < \mu < 2$, with only a single image of the lensed source), and which are inconclusive. We then develop and apply lens models in the visibility plane—as is appropriate for interferometers like the SMA—for all of the objects that show convincing evidence of moderate or strong lensing. This provides measurements of the total (baryonic and non-baryonic) masses within θ_E (M_E), the magnification factors of the background sources at $880\,\mu$m (μ_{880}) and the sizes of the background sources (r_{half}). These are fundamental parameters needed to understand the physics of galaxy evolution at intermediate redshift ($0.2 < z < 1.3$) and high redshift ($z > 1.5$).

In Section 2, we describe our selection technique and present the SMA, MMT, Gemini-S, WHT, and VLT data (highlighting which datasets are new to this paper and which have been published previously). We also show *HST* or Keck adaptive optics (AO) imaging for comparison with the SMA imaging and reference the future papers that will present the *HST* and Keck data. Section 3 contains a description of our lens modeling methodology and a detailed description of each object in the sample. We discuss the implications of the lens modeling for the population of foreground galaxies discovered by *Herschel* and compare to existing surveys for lenses in Section 4. The lens model implications for the lensed SMGs are discussed in Section 5, with an emphasis on the size-scale of star-formation in SMGs at $1.5 < z < 4.5$. Finally, we present our conclusions in Section 6.

Throughout this paper, we assume $H_0 = 71$ km s^{-1} Mpc^{-1}, $\Omega_{m_0} = 0.27$, and $\Omega_{\Lambda_0} = 0.73$.

2. DATA

In this section, we describe how candidate strongly lensed SMGs are selected from wide-field *Herschel* surveys and present SMA high-spatial resolution imaging of the dust continuum emission from these candidate lensed SMGs as well as optical spectroscopy obtained with the MMT, Gemini-S, and WHT. We also highlight ancillary optical and near-IR imaging that is used to determine the position of the lensing galaxy or galaxies and reference the papers that fully present and analyze those data.

2.1. Selection of Candidate Lensed SMGs

The first suggestion that wide-field surveys (i.e., covering $\gtrsim 100$ deg^2) at submm or mm wavelengths would efficiently identify strongly lensed galaxies was made nearly two decades ago (Blain 1996), but it is only in the past few years, with the advent of *Herschel* and the SPT, that such surveys have reached the requisite survey area and sensitivity to discover them in large numbers. We select candidate strongly lensed galaxies from the two widest *Herschel* extra-galactic surveys: H-ATLAS and HerMES. The total area considered for the candidate selection

is ≈ 300 deg^2 in H-ATLAS (comprising the full equatorial fields and $\approx 75\%$ of the northern galactic pole field) and 94.8 deg^2 in nine independent fields in HerMES (for details of the fields, see Oliver et al. 2012). The total area surveyed by *Herschel* as part of H-ATLAS and HerMES is ~ 1000 deg^2 (i.e., roughly a three-fold increase over the area considered for this paper).

An important aspect of candidate lens selection is source extraction and photometry for the *Herschel* Spectral and Photometric Imaging REceiver (SPIRE; Griffin et al. 2010) data. We summarize the relevant aspects of the methodology here and provide references where appropriate.

In the HerMES fields, source detection is achieved by applying the StarFinder code (Diolaiti et al. 2000) to the 250 μm images. Photometry is then computed using the HerMES XID pipeline (Roseboom et al. 2010), which allocates flux density based on the 250 μm position priors obtained with StarFinder.

In the H-ATLAS fields, sources are identified and flux densities are measured using the Multi-band Algorithm for source eXtraction (MADX; S. Maddox et al., in preparation). MADX first subtracts a smooth background, and then filters with the point-spread function (PSF) appropriate for each band. Next, $>2.5\sigma$ peaks are identified in the 250 μm map, and "first-pass" flux density estimates are obtained from the pixel values at these positions in each band. Sub-pixel positions are estimated by fitting to the 250 μm peaks, and more accurate flux-densities are estimated using bi-cubic interpolation to the accurate 250 μm position. In each band, the sources are sorted in order of decreasing flux density using the first-pass pixel values, and a scaled PSF is subtracted from the map before estimation of flux densities for any fainter sources. This step prevents faint source flux densities from being overestimated when they lie near brighter sources. Finally candidate sources are retained in the catalog if their flux densities are more than 5σ in any of the three bands. The 5σ flux density limits in H-ATLAS, including confusion noise (typically ≈ 6 mJy in all three SPIRE bands Nguyen et al. 2010), are 32 mJy at 250 μm, 36 mJy at 350 μm, and 45 mJy at 500 μm (Pascale et al. 2011; Rigby et al. 2011).

Although the HerMES and H-ATLAS teams use different methods to extract photometry, the sources that are the subject of this paper are all high signal-to-noise ratio (S/N), point sources as seen by *Herschel*. In this regime, we expect that the different methods should provide consistent flux density measurements.

The essence of the candidate lens selection technique is to identify objects that are bright at 500 μm. A complete description of the selection technique for the HerMES lens candidates is given by Wardlow et al. (2013). This paper includes the objects tabulated in Wardlow et al. (2013) as well as objects identified in H-ATLAS. We select objects that satisfy $S_{500} > 100$ mJy, a regime that has been shown from previous studies of smaller areas to have relatively little contamination from unlensed SMGs (Negrello et al. 2010; Wardlow et al. 2013). The primary contaminant is local universe galaxies ($z < 0.1$). These galaxies are spatially resolved in SDSS imaging and therefore trivial to remove. There is also a small contamination from blazars, which are non-thermal emitters and are easily removed using data from the NVSS or the Very Large Array Faint Images of the Radio Sky at Twenty-Centimeters survey (FIRST; Becker et al. 1995).

A total of 13 objects in HerMES satisfy $S_{500} > 100$ mJy and are not local galaxies or blazars (Wardlow et al. 2013). In the H-ATLAS fields, there are 91 objects that satisfy these criteria. Considering the combination of the two surveys, this results in a surface density on the sky of ≈ 0.26 deg^{-2}. This value lies

Table 1
Positions and Redshifts of SMA Candidate Strong Gravitational Lens Sample

IAU Name	Short Name	R.A.$_{880}$ (J2000)	Decl.$_{880}$ (J2000)	z_{lens}	Ref.	z_{source}	Ref.	Lens Grade
1HerMES S250 J021830.5−053124	HXMM02	02:18:30.679	−05:31:31.60	1.35 ± 0.01	W13	3.39 ± 0.01	R13	A
1HerMES S250 J022016.5−060143	HXMM01	02:20:16.603	−06:01:43.20	0.6540.502[a]	W13	2.307 ± 0.001	F13	C
H-ATLAS J083051.0+013224	G09v1.97	08:30:51.156	+01:32:24.35	0.6261.002[a]	New	3.634 ± 0.001	R13	A
H-ATLAS J084933.4+021443	G09v1.124	08:49:33.362	+02:14:42.30	0.3478 ± 0.0001	I13	2.410 ± 0.003	H12	C
H-ATLAS J085358.9+015537	G09v1.40	08:53:58.862	+01:55:37.70	. . .	. . .	2.0894 ± 0.0009	L13	B
H-ATLAS J090302.9−014127	SDP17	09:03:03.031	−01:41:27.11	0.9435 ± 0.0009	N10	2.3051 ± 0.0002	L12	A
H-ATLAS J090311.6+003906	SDP81	09:03:11.568	+00:39:06.43	0.2999 ± 0.0002	SDSS	3.042 ± 0.001	F11	A
H-ATLAS J090740.0−004200	SDP9	09:07:40.022	−00:41:59.80	0.6129 ± 0.0005	New	1.577 ± 0.008	L12	A
H-ATLAS J091043.1−000321	SDP11	09:10:43.061	−00:03:22.76	0.7932 ± 0.0012	N10	1.786 ± 0.005	L12	A
H-ATLAS J091305.0−005343	SDP130	09:13:05.107	−00:53:43.05	0.220 ± 0.002	N10	2.6256 ± 0.0005	F11	A
H-ATLAS J091840.8+023047	G09v1.326	09:18:40.927	+02:30:45.90	. . .	. . .	2.5811 ± 0.0012	H12	X
1HerMES S250 J103826.6+581542	HLock04	10:38:26.611	+58:15:42.47	0.61 ± 0.02	W13	. . .	. . .	B
1HerMES S250 J105712.2+565457	HLock03	10:57:12.262	+56:54:58.70	. . .	W13	2.771 ± 0.001	R13	X
1HerMES S250 J105750.9+573026	HLock01	10:57:51.022	+57:30:26.80	0.60 ± 0.04	W13	2.957 ± 0.001	S11	A
H-ATLAS J113526.3−014605	G12v2.43	11:35:26.273	−01:46:06.55	. . .	. . .	3.1276 ± 0.0005	H12	X
H-ATLAS J114637.9−001132	G12v2.30	11:46:37.980	−00:11:31.80	1.2247 ± 0.0001	New	3.2592 ± 0.0010	H12	A
H-ATLAS J125135.4+261457	NCv1.268	12:51:35.412	+26:14:58.63	. . .	. . .	3.675 ± 0.001	K13	B
H-ATLAS J125632.7+233625	NCv1.143	12:56:32.544	+23:36:27.63	0.2551 ± 0.0001	New	3.565 ± 0.001	R13	A
H-ATLAS J132427.0+284452	NBv1.43	13:24:27.206	+28:44:49.40	0.997 ± 0.017	G05	1.676 ± 0.001	G13	C
H-ATLAS J132630.1+334410	NAv1.195	13:26:30.216	+33:44:07.60	0.7856 ± 0.0003	New	2.951 ± 0.001	H13	A
H-ATLAS J132859.3+292317	NAv1.177	13:28:59.246	+29:23:26.13	. . .	. . .	2.778 ± 001	K13	X
H-ATLAS J133008.4+245900	NBv1.78	13:30:08.520	+24:58:59.17	0.4276 ± 0.0003	New	3.1112 ± 0.0001	R13	A
H-ATLAS J133649.9+291801	NAv1.144	13:36:49.985	+29:17:59.77	. . .	. . .	2.2024 ± 0.0002	H12	B
H-ATLAS J134429.4+303036	NAv1.56	13:44:29.518	+30:30:34.05	0.6721 ± 0.0004	New	2.3010 ± 0.0009	H12	A
H-ATLAS J141351.9−000026	G15v2.235	14:13:52.092	−00:00:24.43	0.5470 ± 0.0003	New	2.4782 ± 0.0005	H12	C
H-ATLAS J142413.9+022303	G15v2.779	14:24:13.975	+02:23:03.60	0.595 ± 0.005	B12	4.243 ± 0.001	C11	A
1HerMES S250 J142823.9+352619	HBootes03	14:28:24.074	+35:26:19.35	1.034 ± 0.001	B06	1.325 ± 0.001	B06	C
1HerMES S250 J142825.5+345547	HBootes02	14:28:25.476	+34:55:47.10	0.414 ± 0.001	W13	2.804 ± 0.001	R13	A
1HerMES S250 J143330.8+345439	HBootes01	14:33:30.826	+34:54:39.75	0.59 ± 0.08	W13	3.274 ± 0.001	R13	A
H-ATLAS J144556.1−004853	G15v2.481	14:45:56.297	−00:48:51.70	. . .	. . .	. . .	. . .	X

Notes. Definition of lens grades: A = Obvious strong lensing morphology in SMA map and distinct lens and source redshifts; B = Obvious strong lensing morphology in SMA map, but only a single redshift measurement (either lens or source); C = Evidence for moderate lensing from SMA map and distinct lens and source redshifts; X = SMA imaging and spectroscopic redshifts do not provide conclusive evidence of lensing. Reference key: G05 = Gladders & Yee (2005); B06 = Borys et al. (2006); N10 = Negrello et al. (2010); S11 = Scott et al. (2011); F11 = Frayer et al. (2011); C11 = Cox et al. (2011); H12 = Harris et al. (2012); B12 = Bussmann et al. (2012); L12 = Lupu et al. (2012); W13 = Wardlow et al. (2013); I13 = Ivison et al. (2013); G13 = R. D. George et al. (in preparation); R13 = D. A. Riechers et al. (in preparation); K13 = M. Krips et al. (in preparation); L13 = R. E. Lupu et al. (in preparation); H13 = A. I. Harris et al. (in preparation).
[a] Multiple lens redshifts have been measured for these targets. The redshift uncertainty is 0.001 in all cases.

between the values of 0.32 deg^{-2} from Negrello et al. (2010) and 0.14 ± 0.04 deg^{-2} from Wardlow et al. (2013), as expected since it represents a combination and extension of these previous efforts. Cosmic variance likely explains the difference in the surface densities of lenses between HerMES and H-ATLAS. A detailed calculation of this effect requires taking into account the cosmic variance of both the lensed SMGs and the lenses themselves and is beyond the scope of this paper.

Efforts are on-going to obtain a complete database of follow-up observations for this sample of 104 candidate lensed SMGs. The present paper focuses on a subset of 30 candidates with superb existing follow-up observations (hereafter, we refer to this as the "SMA subsample"). These targets were initially selected on the basis of strong 1.2 mm detections from the Max Planck Millimeter Bolometer (MAMBO) array (Kreysa et al. 1998) at the Institut de Radioastronomie Millimétrique (IRAM) 30 m telescope (H. Dannerbauer et al. in preparation). Subsequent follow-up efforts have now provided high-spatial resolution 880 μm imaging with the SMA, spectroscopic redshifts of the lensed SMGs obtained with GBT, CSO, CARMA, PdBI, and *Herschel* (Cox et al. 2011; Harris et al. 2012; Lupu et al. 2012, D. A. Riechers et al., in preparation; M. Krips et al., in

preparation, George et al. 2013), and spectroscopic redshifts to the lenses obtained with the MMT, Gemini-S, or WHT. In addition, Keck-II Near InfraRed Camera 2 (NIRC2) laser guide star adaptive optics (LGSAO) imaging has been obtained for nearly half of the candidate lensed SMG sample (Wardlow et al. 2013; J. Calanog et al., in preparation). These datasets provide the information needed to confirm the lensing hypothesis and begin analysis of the source and lens properties. Table 1 provides basic positional data for the SMA subsample, including the International Astronomical Union names, short names to aid comparison with previous publications, positions measured from the SMA 880 μm image (see Section 2.2), and redshift measurements for the lens(es) (see Sections 2.3, 2.4, 2.5, 2.6, and references in the table) and background sources (references given in the table), where available.

Figure 1 shows the S_{350}/S_{500} SPIRE colors as a function of S_{500} flux density for all galaxies in the H-ATLAS phase I catalog with S/N > 3 in all SPIRE bands (grayscale, logarithmic scaling), the full sample of 104 candidate *Herschel* lensed SMGs in HerMES and H-ATLAS (cyan squares), the SMA subsample with superb follow-up data that is the focus of this paper, and a sample of objects selected from the SPT survey with published
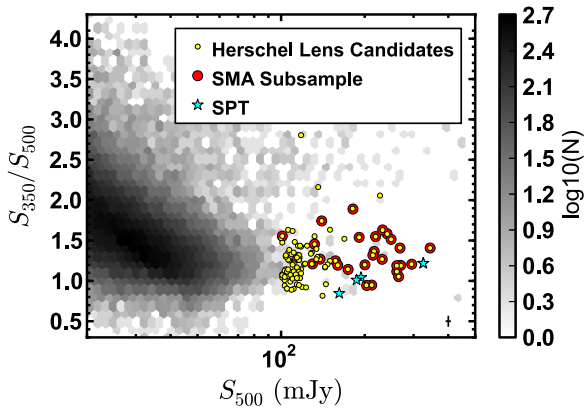
Figure 1. *Herschel*/SPIRE photometry of all galaxies in the H-ATLAS phase I catalog with S/N > 3 at 250 μm, 350 μm, and 500 μm (grayscale). The sample of H-ATLAS and HerMES sources that satisfy the selection criteria used to select lens candidates are overplotted with yellow filled squares. The targets presented in this paper are represented by red filled circles ("SMA subsample"), and a comparison sample of lensed SMGs discovered by the SPT that have published lens models are represented by cyan stars. Representative error bars are shown in the lower right corner. The SMA subsample is biased toward higher 500 μm flux densities but has similar S_{350}/S_{500} and S_{250}/S_{350} colors (not shown).

(A color version of this figure is available in the online journal.)

lens models (Hezaveh et al. 2013). The SMA subsample is biased to higher S_{500} values than the full sample. We therefore expect the lensing rate to be higher than in the full sample. The SPIRE colors (S_{350}/S_{500} and S_{250}/S_{350}) are comparable between the full sample and the SMA subsample. The SMA subsample contains nearly all galaxies in the parent sample with $S_{500} > 170$ mJy (the lone exception is H-ATLAS J1429−002, which has the highest S_{350}/S_{500} ratio in the full lens candidate sample and is the subject of a study based on data from the Atacama Large Millimeter/submillimeter Array (ALMA) and other facilities; H. Messias et al., in preparation).

2.2. SMA Imaging

SMA data were obtained over a period of multiple semesters from 2010 March through 2013 May with a total of 162 hr of on-source integration time. Each target was typically observed in multiple array configurations with $t_{int} = 1$–2 hr on-source per configuration. We used track-sharing of multiple targets per track to ensure the best possible *uv* coverage.

Observations took place in a range of conditions from superb (atmospheric opacities of $\tau_{225 \, GHz} = 0.04$, phase errors of $\Delta(\phi_{rms}) = 10°$) to good (atmospheric opacities of $\tau_{225 \, GHz} = 0.1$, phase errors of $\Delta(\phi_{rms}) = 40°$). Phase errors are estimated from a fixed monitoring system on a variety of baselines. For some of the observations, 1 or more antennas were unavailable, so in those cases the total number of antennas (N_{ant}) used was less than 8. Most notably, in early 2011, the lower sideband of the SMA 345 GHz receiver in antenna 1 was flagged due to significant instrumental noise. In general, we optimized the SMA single-polarization 345 GHz receivers for continuum detection by tuning to a frequency of $\nu_{LO} \approx 340$ GHz. In some cases ν_{LO} varied from this value by up to 10 GHz to avoid retuning in the middle of the night when the SMA switched from another program. Table 2 presents details regarding the SMA observations, including the date, array configuration, local oscillator frequency (ν_{LO}), $\tau_{225 \, GHz}$, ϕ_{rms}, N_{ant}, t_{int}, and original reference (some of the data used in this paper were originally presented elsewhere).

The SMA receivers make use of an intermediate frequency coverage of 4 GHz, providing a total of 8 GHz bandwidth (considering both sidebands), with a center-to-center sideband separation of 12 GHz. The primary goal of the observations is to detect the continuum emission at the highest possible significance. When a spectroscopic redshift for a *Herschel* source was available, we tuned the receivers to the closest CO rotational transition, as long as the S/N of the continuum data would not be compromised by doing so. This was possible for 8 of our targets. Since the background galaxies lie at $1.5 < z < 4.5$, our observations probe emission from the $J = 10$ (or higher) levels in lines that are typically faint in SMGs and therefore difficult to detect. We defer a discussion of the molecular line measurements based on the SMA data to a future publication.

Bandpass calibrators were chosen primarily based on their 880 μm flux densities (where possible, we used calibrators with $S_{880} > 5$ Jy) and their observability at the beginning or end of each night. For absolute flux density calibration, Titan was used whenever possible, followed by Callisto, Neptune (in subcompact array only), and MWC349A (when no planets or moons were available). Amplitude and phase gain calibration was achieved by monitoring nearby (angular separation from science target of <15°), bright ($S_{880} > 0.5$ Jy) quasars. Whenever possible, we used multiple quasars for gain calibration, including a fainter quasar ($S_{880} > 0.1$ Jy) much closer to the science target (angular separation <5°) to provide an independent check of the reliability of the calibration, particularly phase transfer. We used the Interactive Data Language (IDL) MIR package to calibrate the *uv* visibilities.

We used the Multichannel Image Reconstruction, Image Analysis, and Display (MIRIAD) software package (Sault et al. 1995) to reconstruct and deconvolve the image from the visibilities. We used natural weighting to achieve maximum sensitivity for all targets. We combine visibility data from all available configurations for each target. The beam size and shape in the resulting images vary greatly from target to target. This is primarily because not every target was observed in all array configurations, but there is also some dependence on the declination of the target, because the SMA *uv* coverage is less complete at declinations near 0°. In general, we achieve spatial resolutions of $\approx 0\farcs6$ FWHM.

Figure 2 shows the SMA image of each object in the SMA subsample (red contours, beginning at $\pm 3\sigma$ and increasing by factors of $\sqrt{2}$) in comparison with the best available optical or near-IR image (grayscale; see Section 2.7). A detailed source-by-source description is deferred to Section 3.2. The position of the 880 μm emission centroid (estimated by-eye) for each source is presented in Table 1. There is no absolute significance to these centroid values, but they are necessary to undertake lens modeling.

We use the SMA images in conjunction with knowledge of the redshifts of the lenses and sources (see Sections 2.3, 2.4, 2.5, and 2.6 for details) to characterize the nature of the lensing that is occurring in the SMA subsample. Those galaxies showing multiple images with a morphology typical of strong lensing and that have known distinct lens and source redshifts are given an A grade. Galaxies with obvious strong lensing morphology but with only a single known redshift measurement (either of the lens or the source) receive a B grade. We expect that all B grade systems are strong lenses, but without distinct redshift measurements we cannot be certain. Galaxies showing only a single image of the background source, but with known distinct

Table 2
SMA Observations

IAU Name	Reference	UT Date	Array Configuration[a]	ν_{LO} (GHz)	$\tau_{225\,GHz}$	$\Delta(\phi_{rms})$ (deg)	N_{ant}	t_{int} (hr)
J021830.5−053124	I11	2009 Dec 10	COM	339.925	0.10	20	7	3.7
. . .	W13	2010 Sep 25	EXT	342.003	0.10	30	7	2.0
. . .	New	2011 Jan 26	VEX	343.160	0.08	10	6.5[b]	1.9
J022016.5−060143	W13	2010 Aug 14	SUB	342.017	0.07	10	8	0.9
. . .	W13	2010 Sep 26	EXT	342.001	0.07	20	7	2.5
. . .	F13	2011 Jan 4	VEX	340.226	0.06	25	6.5[b]	3.2
J083051.0+013224	New	2011 Dec 8	COM	339.564	0.09	20	8	1.4
. . .	New	2012 Feb 4	EXT	339.946	0.04	20	8	2.4
J084933.4+021443	I13	2011 Dec 8	COM	339.564	0.09	20	8	1.4
. . .	I13	2012 Jan 31	EXT	339.537	0.05	30	7	4.9
. . .	I13	2012 Mar 31	VEX	339.917	0.05	25	7	1.7
J085358.9+015537	New	2011 Dec 8	COM	339.564	0.09	20	8	1.4
. . .	New	2012 Feb 4	EXT	339.946	0.04	20	8	2.4
. . .	New	2012 Mar 31	VEX	339.917	0.05	25	7	1.7
. . .	New	2012 Apr 9	VEX	339.915	0.05	10	7	1.3
J090302.9−014127	New	2010 Dec 16	COM	342.410	0.13	20	7.5[b]	1.5
. . .	New	2011 Jan 30	EXT	340.244	0.05	20	6.5[b]	1.7
. . .	New	2011 Jan 26	VEX	343.160	0.08	35	6.5[b]	2.0
. . .	New	2012 Apr 9	VEX	339.915	0.05	10	7	1.3
J090311.6+003906	N10	2010 Mar 16	SUB	340.725	0.05	10	5	2.5
. . .	N10	2010 Apr 9	COM	341.609	0.07	25	6	2.6
. . .	N10	2010 Apr 20	COM	340.714	0.06	30	7	2.4
. . .	N10	2010 Feb 25	VEX	340.735	0.10	40	8	5.0
J090740.0−004200	New	2010 Dec 16	COM	342.410	0.13	20	7.5[b]	1.5
. . .	New	2011 Jan 30	EXT	340.244	0.05	20	6.5[b]	1.7
. . .	New	2012 Feb 6	EXT	339.989	0.05	30	8	0.9
J091043.1−000321	New	2010 Dec 16	COM	342.410	0.13	20	7.5[b]	1.5
. . .	New	2011 Jan 30	EXT	340.244	0.05	20	6.5[b]	1.7
. . .	New	2012 Feb 7	EXT	339.993	0.04	15	8	2.0
. . .	New	2011 Jan 26	VEX	343.160	0.08	35	6.5[b]	2.0
J091305.0−005343	N10	2010 Mar 16	SUB	340.725	0.05	10	5	2.5
. . .	N10	2010 Apr 9	COM	341.609	0.07	25	6	2.6
. . .	N10	2010 Apr 20	COM	340.714	0.06	30	7	2.4
. . .	N10	2010 Feb 28	VEX	340.735	0.07	5	7	5.0
J091840.8+023047	New	2012 Feb 6	EXT	339.989	0.05	30	8	0.9
. . .	New	2012 Feb 7	EXT	339.993	0.04	15	8	2.0
J103826.6+581542	W13	2010 May 16	COM	341.981	0.06	35	7	3.8
J105712.2+565457	W13	2010 Dec 6	COM	338.148	0.05	10	8	1.1
. . .	New	2011 Jan 4	VEX	340.226	0.08	20	6.5[b]	2.1
J105750.9+573026	C11	2010 May 14	COM	340.742	0.06	10	7	4.2
. . .	New	2011 Jan 4	VEX	340.226	0.08	20	6.5[b]	2.1
J113526.3−014605	New	2012 Feb 4	EXT	339.946	0.04	20	8	1.3
J114637.9−001132	F12	2012 Jan 14	SUB	336.929	0.15	20	7	2.0
. . .	F12	2011 May 22	COM	339.579	0.08	25	7	1.0
. . .	New	2012 Feb 4	EXT	339.946	0.04	20	8	1.3
J125135.4+261457	New	2012 May 22	COM	339.579	0.09	35	7	1.7
. . .	New	2012 Feb 6	EXT	339.989	0.05	30	8	1.2
J125632.7+233625	New	2012 May 25	COM	340.045	0.08	20	7	0.8
. . .	New	2012 Feb 6	EXT	339.989	0.05	30	8	1.2
J132427.0+284452	F13a	2011 Dec 15	COM	339.561	0.05	10	8	3.0
. . .	F13a	2012 Jan 31	EXT	339.537	0.05	30	7	4.4
. . .	F13a	2012 Apr 9	VEX	339.915	0.05	10	7	2.3
J132630.1+334410	New	2012 Feb 7	EXT	339.993	0.04	15	8	1.4
J132859.3+292317	New	2013 May 3	SUB	340.757	0.12	25	6	0.8
. . .	New	2012 Feb 7	EXT	339.993	0.04	15	8	1.4
. . .	New	2012 Apr 24	VEX	339.960	0.06	20	7	2.5
J133008.4+245900	New	2012 May 25	COM	340.045	0.08	20	7	0.8
. . .	New	2012 Feb 7	EXT	339.993	0.04	15	8	1.4
J133649.9+291801	New	2013 May 3	SUB	340.757	0.12	25	6	0.8
. . .	New	2012 Feb 6	EXT	339.989	0.05	30	8	1.2
. . .	New	2012 Apr 24	VEX	339.960	0.06	20	7	2.5
J134429.4+303036	New	2011 May 22	COM	339.579	0.09	35	7	1.7
. . .	New	2011 Jul 26	EXT	341.037	0.06	15	8	1.7
. . .	New	2012 Mar 17	EXT	339.949	0.04	35	7	3.2
. . .	New	2012 Apr 9	VEX	339.915	0.05	10	7	2.3

Table 2
(Continued)

IAU Name	Reference	UT Date	Array Configuration[a]	ν_{LO} (GHz)	$\tau_{225\,GHz}$	$\Delta(\phi_{rms})$ (deg)	N_{ant}	t_{int} (hr)
J141351.9−000026	New	2011 May 23	COM	339.544	0.06	30	7	2.9
. . .	New	2011 Jan 30	EXT	340.244	0.05	20	6.5[b]	1.1
. . .	New	2011 Jan 24	VEX	341.449	0.04	10	5.5[b]	1.6
. . .	New	2011 Jan 26	VEX	343.160	0.09	30	6.5[b]	1.3
J142413.9+022303	B12	2010 Jun 16	COM	342.100	0.10	30	8	3.0
. . .	B12	2011 Jan 28	EXT	340.711	0.08	30	6.5[b]	1.3
. . .	B12	2011 Jan 4	VEX	340.226	0.10	20	6.5[b]	1.8
. . .	B12	2011 Jan 6	VEX	340.225	0.04	10	6.5[b]	1.7
J142823.9+352619	New	2011 Jan 28	EXT	340.711	0.08	10	6.5[b]	1.0
. . .	New	2011 Feb 4	EXT	350.086	0.12	35	7	1.3
J142825.5+345547	W13a	2012 May 25	COM	340.045	0.08	20	7	0.8
. . .	W13a	2011 Jul 26	EXT	341.037	0.06	15	8	1.7
J143330.8+345439	W13	2010 Dec 16	COM	342.410	0.11	20	7.5[b]	0.8
. . .	W13	2011 Jan 28	EXT	340.711	0.08	10	6.5[b]	1.0
. . .	W13	2011 Feb 4	EXT	350.086	0.12	35	7	1.3
J144556.1−004853	New	2011 May 23	COM	339.544	0.06	30	7	2.9
. . .	New	2011 Jan 30	EXT	340.244	0.05	20	6.5[b]	1.1
. . .	New	2011 Jan 26	VEX	343.160	0.09	30	6.5[b]	1.3

Notes. References key: N10 = Negrello et al. (2010); C11 = Conley et al. (2011); I11 = Ikarashi et al. (2011); F12 = Fu et al. (2012); B12 = Bussmann et al. (2012); W13 = Wardlow et al. (2013); F13 = (Fu et al. 2013); I13 = Ivison et al. (2013); W13a = J. L. Wardlow et al. (in preparation); F13a = H. Fu et al. (in preparation).
[a] SUB = subcompact (longest baseline length ≈25 m); COM = compact (longest baseline length ≈75 m); EXT = extended (longest baseline length ≈220 m); VEX = very extended (longest baseline length ≈510 m).
[b] The lower sideband of one antenna was flagged for these observations.

lens and source redshifts, are given a C grade. Finally, an X grade is given to those objects where the SMA imaging and the available spectroscopic redshifts provide inconclusive evidence of lensing. Additional data are needed to determine whether lensing is occurring in these objects. Our grades are listed in Table 1.

We compute total flux densities at 880 μm within rectangular apertures customized to match the spatial extent of each object in the SMA images. Uncertainties on these measurements are derived by placing apertures of the same size and shape at random, non-overlapping locations within the SMA primary beam field of view (excluding regions containing flux density from the source) and computing the 1σ root-mean-square variation (which is generally well-described by a Gaussian) in the distribution of aperture flux densities. The number of apertures varied from target to target, but was typically ≈100.

2.3. MMT Optical Spectroscopy

Long-slit spectroscopic observations using the MMT Red Channel Spectrograph (Schmidt et al. 1989) were conducted in the 2012A semester (PI: R. S. Bussmann) and provided data on H-ATLAS J125632.7+233625, H-ATLAS J132630.1+334410, H-ATLAS J133008.4+245900, and H-ATLAS J134429.4+303036. The total on-source integration times for these targets were 70–120 minutes apiece. The observations were obtained during dark time in near-photometric conditions and seeing was typically 1″0–1″5. Details of the observations for each target are given in Table 3.

We obtained lamp flats for all targets at the beginning of each night for flat fields. We obtained a sequence of up to six consecutive 10 minute exposures on each target. For wavelength calibration, before and after each of these sequences we obtained comparison lamp observations using a He/Ar/Ne comparison lamp. We checked the focus periodically throughout the night.

We used either the 270 or the 300 lines per mm grating with a central wavelength ($\lambda_{central}$) of 6996 Å or 5504 Å. The slit width was chosen to be as small as atmospheric seeing allowed and was either 1″5 or 2″0. The spectral resolution at $\lambda_{central}$ ($\Delta\lambda$) was 10–30 Å.

The long-slit data were reduced using standard IRAF one-dimensional spectroscopy routines. The primary aim of these observations for the purpose of this paper is to obtain a spectroscopic redshift for the putative lensing system. We accomplished this task with the XCSAO routine in IRAF, using as a template a 5 Gyr old simple stellar population from Bruzual & Charlot (2003) with solar metallicity and a Chabrier initial mass function (IMF). This template does not perfectly match the lensing galaxy spectra, but it is sufficient to determine a robust redshift. The lens redshifts are presented in Table 1. A more detailed exploration of the optical spectra is deferred to a subsequent publication, so we do not show the spectra in this paper.

2.4. Gemini-South Optical Spectroscopy

Long-slit spectroscopic observations using the Gemini Multi-Object Spectrograph-South (GMOS-S; Hook et al. 2004) were conducted in queue mode during the 2012A semester as part of program GS-2012A-Q-52 (PI: R. S. Bussmann) and provided data on H-ATLAS J090740.0−004200 and H-ATLAS J141351.9−000026. The total on-source integration times for each of these targets were 1–4 hr. The observations were obtained during dark time in near-photometric conditions. Observational details are given in Table 3.

Some aspects of the observing strategy were common to both targets and followed the guidelines given by the Gemini observatory.[34] Flat field observations were interspersed between

---

[34] http://www.gemini.edu/sciops/instruments/gmos/calibration
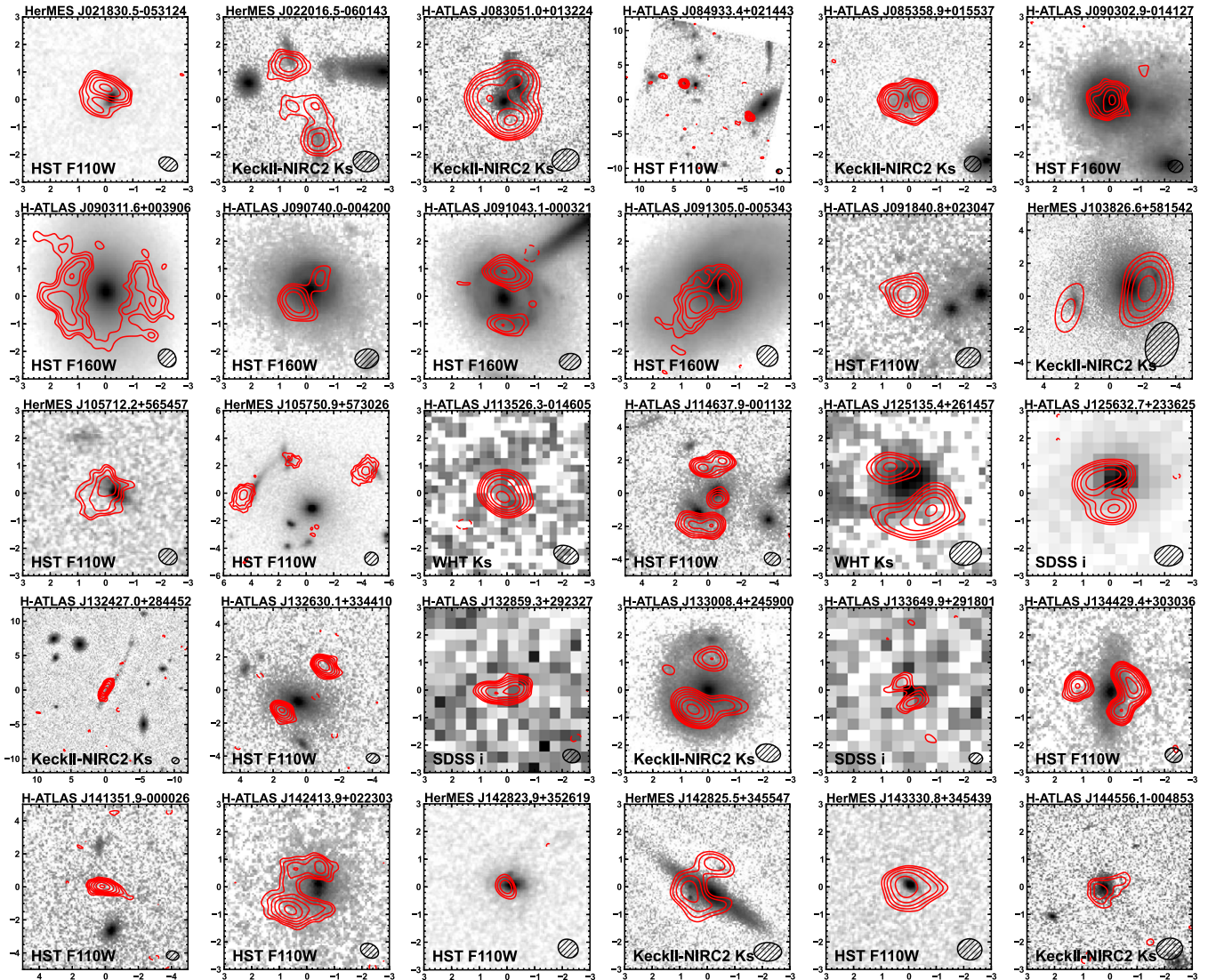
Figure 2. SMA 880 μm images (red contours, starting at $\pm 3\sigma$ and increasing by factors of $\sqrt{2}$) of candidate lensed SMGs from H-ATLAS and HerMES, overlaid on best available optical or near-IR images (logarithmic scaling; telescope and filter indicated in lower left corner of each panel). North is up and East is left, with axes having units of arcseconds relative to the 880 μm centroid as given in Table 1. The elliptical FWHM of the SMA's synthesized beam is shown in the lower right corner of each panel. The image separations are $\approx$1–2$''$, suggesting gravitational potential wells typical of isolated galaxies or small numbers of galaxies for the lenses (only two lensed sources are associated with galaxy clusters: J132427.0+284452 and J141351.9−000026).

(A color version of this figure is available in the online journal.)

Table 3
Optical Spectroscopy Observations

IAU Name	Telescope	UT Date	Grating (lines mm^{-1})	$\lambda_{\mathrm{central}}$ (Å)	Slit Width ($''$)	$\Delta\lambda$ (Å)	t_{int} (min)
J083051.0+013224	WHT	2011 Apr 24	400	6500	1.0	15	60
J090740.0−004200	Gemini-S	2012 Feb 26	400	6710	1.5	10.5	120
J114637.9−001132	X-Shooter	2012 Sep 18/19	. . .	16200	1.0	3.0	320
J125632.7+233625	MMT	2012 Feb 23	300	5504	1.5	17.9	80
J132630.1+334410	MMT	2012 Feb 23	270	6996	2.0	21.9	120
J133008.4+245900	MMT	2012 Feb 23	300	5504	1.5	16.4	70
J134429.4+303036	MMT	2012 Feb 22	270	6996	1.5	17.9	80
J141351.9−000026	Gemini-S	2012 Feb 26	150	6720	1.5	22.3	240

the science exposures at each wavelength setting. CuAr arc lamp exposures were taken for the purpose of wavelength calibration, using the same instrumental setup as for the science exposures. A 5 Å spectral dither between exposures was used to cover the gap in the GMOS-S chip, and we binned the CCD pixels by a

factor of 4 in both the spatial and spectral directions, providing a spatial scale of 0$''$.288 pixel^{-1} and a spectral pixel scale of 2.69 Å. We used the GG455 blocking filter. Aspects of the observing strategy that varied from target to target are given in Table 3.

The long-slit data were reduced using the IRAF Gemini GMOS reduction routines, following the standard GMOS-S reduction steps in the example taken from the Gemini observatory webpage.[35] We used the same procedure as outlined in Section 2.3 to measure a spectroscopic redshift using IRAF's xcsao task. The lens redshifts are presented in Table 1. We plan a detailed exploration of the optical spectra in future work, so we do not show the optical spectra in this paper.

2.5. WHT Optical Spectroscopy

Long-slit spectroscopic observations using the auxiliary port camera (ACAM; Benn et al. 2008) at the WHT were conducted in the 2011A semester (PIs: I. Pérez-Fournon and A. Verma) and provided three 1200 s exposures of H-ATLAS J083051.0+013224 on 2011 April 24. ACAM provides fixed-format spectroscopy, covering a spectral range of 3500–9400 Å (spectral resolution of ≈ 3.3 Å pix^{-1}) using a 400 lines mm^{-1} transmission Volume Phase Holographic grating. The observing conditions were photometric and the seeing was $0\rlap{.}''75$. We have included the observational details for this target in Table 3 for completeness.

We obtained Tungsten lamp flats at the beginning of each night for flat fields. For wavelength calibration, we obtained comparison lamp observations using a CuNe lamp. We checked the focus periodically throughout the night using the ACAM imaging mode.

A position angle of 114 deg east of north was chosen to include several objects visible on the optical imaging close to the candidate lensing galaxy. The slit width was $1\rlap{.}''0$ and the corresponding spectral resolution provided by the grating was $R \approx 450$, or 15 Å FWHM at 6750 Å.

The long-slit spectroscopic data were reduced using standard IRAF two-dimensional spectroscopy programs to correct for the distortions in the data and apply the wavelength and flux density calibration.

The ACAM spectroscopy, based on G-band and Mg absorption features, shows that the primary lens (i.e., the galaxy that is closest to the SMA emission centroid) is located at $z_{\mathrm{lens}} = 0.626 \pm 0.001$. A nearby disk-like galaxy was detected in the acquisition images and spatially resolved from the primary lens (the existence of this additional galaxy is confirmed by ancillary high-spatial resolution imaging from Keck-II adaptive optics imaging; see Section 2.7). In the ACAM long-slit spectra an emission line is detected at 7462 Å at the spatial location of the disk-like galaxy. We cannot associate this line with emission lines at the same redshift as the primary lens. The most plausible identification is [O II]3727 at $z = 1.002 \pm 0.001$, in which case the two galaxies are at different redshifts.

2.6. VLT X-Shooter Spectroscopy

The optical and near-IR spectra of the southeastern lens in J114637−001132 (i.e., the galaxy denoted as "G2" by Fu et al. 2012) were obtained with the X-shooter spectrograph (Vernet et al. 2011) at the VLT. X-shooter provides simultaneous spectral coverage from 300 nm to 2.5 μm. The $1'' \times 11''$ slit was used in the "UVB" arm (300–560 nm), while the $0\rlap{.}''9 \times 11''$ slits were used in the "VIS" arm (550–1020 nm) and "NIR" arm (1020–2480 nm), yielding a resolving power of $\lambda/\Delta\lambda$ of 4350, 7450 and 5300 in the three bands, respectively. The observations were obtained on 2012 September 18 and 19. The

total integration time was 320 minutes and comprised individual exposures of 20 minutes each. The object was nodded along the slit by a few arcsec between one exposure and the next.

Data reduction was performed by following the standard steps of the public X-shooter pipeline (Goldoni et al. 2006). Sky emission lines were subtracted by exploiting temporally contiguous exposures in which the objects was nodded in a different position of the slit. After flat-fielding, the pipeline extracts the different orders of the echelle spectrum, which are then rectified, wavelength calibrated and merged. Then the spectra were calibrated in flux by using the observation of a spectrophotometric standard. The final mono-dimensional spectrum was extracted from an aperture of $1''$.

The lensing galaxy G2 is clearly detected with several emission lines ([O III],Hb,Ha,[N II],[S II], [O II]) that imply a redshift of $z_{\mathrm{lens}} = 1.2247$.

2.7. Ancillary Optical and Near-IR Imaging

In all cases where the SMA has clearly resolved multiple images of the background source, there is no evidence for submm emission from the lens. This means that detection of the foreground lens requires observations at optical or near-IR wavelengths. This paper makes use of the best available optical or near-IR imaging to pinpoint the location of the lens and determine whether it comprises multiple galaxies. This imaging is shown in grayscale in Figure 2, and the telescope and filter used are given in the lower left corner of each panel. Fifteen objects use *HST* Snapshot imaging (marked as "*HST* F110W" in Figure 2), five use Keck-II/NIRC2-LGSAO imaging (marked as "Keck-II_NIRC2 Ks" in Figure 2), five use full-orbit *HST* imaging (marked as "*HST* F160W" in Figure 2), four use SDSS i-band imaging (marked as "SDSS i" in Figure 2), and two use WHT K_{s}-band imaging (marked as "WHT Ks" in Figure 2).

The focus of this paper is lens modeling of the SMA data. A detailed analysis of the optical and near-IR imaging will appear in a set of papers specific to the *HST* Snapshot imaging (S. Amber et al., in preparation; J. Calanog et al. in preparation), the full-orbit *HST* imaging (M. Negrello et al., in preparation, S. Dye et al., in preparation), and the Keck-II/NIRC2-LGSAO imaging (J. Calanog et al., in preparation) and the WHT K_{s} imaging (P. Martínez-Navajas et al., in preparation).

To facilitate comparison with existing surveys for lenses based on SDSS spectroscopy (e.g., Bolton et al. 2008; Brownstein et al. 2012), we compute i-band photometry using SDSS Data Release 9 (DR9) for all of the objects in the SMA subsample. The imaging aspect of DR9 provides five optical bands: u, g, r, i, and z. The 95% completeness levels for point sources are $u = 22.0$, $g = 22.2$, $r = 22.2$, $i = 21.3$, and $z = 20.5$ (AB mag), corresponding to flux densities of 5.7 μJy, 4.8 μJy, 4.8 μJy, 11.0 μJy, and 23.0 μJy, respectively. The median seeing in the images at r-band is typically $1\rlap{.}''3$.

We searched for counterparts in the DR9 catalog within a $2''$ radius of each expected lens position based on the best available optical or near-IR imaging. If a counterpart was found, then it was assigned photometry directly from the DR9 catalog. If no counterpart was found, we used our own custom aperture photometry code to measure the 2σ limiting flux density at the position of the target (note that at these wavelengths, the lens is typically much brighter than the source). We used a $4''$ diameter circular aperture and computed the sky background in an annulus with an inner radius of $2''$ and an outer radius of $5''$. We measured the uncertainties by placing N random apertures (where $N \approx 300$) of the same size and shape within $3'$ of

---

Table 4
Spatially Integrated Flux Densities of Strong Lens Sample[a]

IAU Name	i[b] (AB mag)	S_{250} (mJy)	S_{350} (mJy)	S_{500} (mJy)	S_{880} (mJy)
J021830.5−053124	>22.6	92 ± 7	122 ± 8	113 ± 7	66.0 ± 5.4
J022016.5−060143	20.32 ± 0.06	180 ± 7	192 ± 8	132 ± 7	28.3 ± 3.4
J083051.0+013224	20.85 ± 0.09	260 ± 7	321 ± 8	269 ± 9	85.5 ± 4.0
J084933.4+021443	19.01 ± 0.02	242 ± 7	293 ± 8	231 ± 9	50.0 ± 3.5
J085358.9+015537	>22.3	389 ± 7	381 ± 8	241 ± 9	61.4 ± 2.9
J090302.9−014127	20.92 ± 0.11	347 ± 7	339 ± 8	219 ± 9	54.7 ± 3.1
J090311.6+003906	18.17 ± 0.01	138 ± 7	199 ± 8	174 ± 9	78.4 ± 8.2
J090740.0−004200	20.94 ± 0.07	471 ± 7	343 ± 8	181 ± 9	24.8 ± 3.3
J091043.1−000321	21.41 ± 0.09	417 ± 6	378 ± 7	232 ± 8	30.6 ± 2.4
J091305.0−005343	18.74 ± 0.02	116 ± 6	140 ± 7	108 ± 8	36.7 ± 3.9
J091840.8+023047	>22.4	142 ± 7	175 ± 8	138 ± 9	18.8 ± 1.6
J103826.6+581542	18.71 ± 0.02	191 ± 7	157 ± 10	101 ± 7	30.2 ± 2.2
J105712.2+565457	22.0 ± 0.4	114 ± 7	147 ± 10	114 ± 7	50.3 ± 5.9
J105750.9+573026	20.15 ± 0.04	403 ± 7	377 ± 10	249 ± 7	55.7 ± 5.8
J113526.3−014605	>22.5	290 ± 7	295 ± 8	216 ± 9	48.6 ± 2.3
J114637.9−001132	21.44 ± 0.10	290 ± 6	356 ± 7	295 ± 8	86.0 ± 4.9
J125135.4+261457	>22.2	145 ± 7	201 ± 8	212 ± 9	78.9 ± 4.4
J125632.7+233625	18.70 ± 0.02	214 ± 7	291 ± 8	261 ± 9	97.2 ± 6.5
J132427.0+284452	>22.6	347 ± 7	377 ± 8	268 ± 9	30.2 ± 2.2
J132630.1+334410	20.25 ± 0.07	179 ± 7	279 ± 8	265 ± 9	65.2 ± 2.3
J132859.3+292327	>22.6	264 ± 9	310 ± 10	261 ± 10	50.1 ± 2.1
J133008.4+245900	20.00 ± 0.03	273 ± 7	282 ± 8	214 ± 9	59.2 ± 4.3
J133649.9+291801	>22.7	295 ± 8	294 ± 9	191 ± 10	36.8 ± 2.9
J134429.4+303036	20.88 ± 0.06	481 ± 9	484 ± 13	344 ± 11	73.1 ± 2.4
J141351.9−000026	22.0 ± 0.2	190 ± 7	240 ± 8	200 ± 9	33.3 ± 2.6
J142413.9+022303	21.62 ± 0.12	115 ± 7	192 ± 8	203 ± 9	90.0 ± 5.0
J142823.9+352619	22.2 ± 0.4	323 ± 6	244 ± 7	140 ± 33	18.4 ± 2.5
J142825.5+345547	19.89 ± 0.04	159 ± 6	196 ± 7	157 ± 33	42.3 ± 4.7
J143330.8+345439	>22.3	158 ± 6	191 ± 7	160 ± 33	59.6 ± 3.9
J144556.1−004853	>22.7	141 ± 7	157 ± 8	130 ± 9	9.0 ± 2.1

Notes.
[a] Measurement uncertainties for *Herschel* photometry do not include absolute flux density calibration uncertainty of 7%.
[b] *i*-band magnitudes obtained from SDSS DR9.

the lens candidate (taking care to avoid any objects found in the DR9 catalog) and computing the 68% confidence interval of the dispersion in the measured flux densities. The *i*-band AB magnitudes are reported in Table 4 (limits indicate 2σ values), along with the *Herschel*/SPIRE and SMA $880\,\mu$m measurements (the values reported in the table do not include absolute flux density calibration uncertainty of 7%).

3. LENS MODELS

The SMA data provide sufficient sensitivity and spatial resolution to permit tight constraints on parameters of the lens models for a total of 25 lensed SMGs out of the SMA subsample of 30 (those labeled with grade A, B, or C in Table 1). For some of these objects, deep *HST* or Keck-II/NIRC2-LGSAO data exist that permit the assembly of lens models which take into account simultaneously the optical, near-IR, and submm data. However, because this sample of lensed SMGs are at $z > 1.5$ and are heavily obscured by dust, the lensed emission is frequently detected only in the SMA data and not in the optical or near-IR. Therefore, for the current analysis we focus our efforts on lens models based solely on SMA data (for the handful of exceptions, see Section 3.1 for details) and defer full spectral energy distribution (SED) lens modeling to subsequent publications. We describe the methodology behind the lens modeling in Section 3.1 and give a detailed discussion of each object in Section 3.2. We defer an examination of the ensemble

properties of the lenses and lensed sources to Sections 4 and 5, respectively.

3.1. Methodology

The SMA is an interferometer, so the surface brightness map of each lensed SMG is obtained with incomplete sampling of the *uv* plane. This means that surface brightness is not necessarily conserved and that the pixel-to-pixel errors in the surface brightness map are correlated. For these reasons, it is important to compare model and data visibilities rather than surface brightness maps. We follow the methodology used in Bussmann et al. (2012), who presented the first lens model derived from a visibility-plane analysis of interferometric imaging of a strongly lensed SMG discovered in wide-field submm surveys. We summarize important details here and refer the interested reader to Bussmann et al. (2012) for further information.

We use the publicly available Gravlens software (Keeton 2001) to map emission from the source plane to the image plane for a given lensing mass distribution. To represent the lens mass profile, we use $N_{\rm lens}$ singular isothermal ellipsoid (SIE) profiles, where $N_{\rm lens}$ is the number of lensing galaxies found from the best available optical or near-IR imaging (a multitude of evidence supports the SIE as a reasonable choice; for a recent review, see Treu 2010).

The source(s) are assumed to have Sérsic profile morphologies (Sersic 1968). We always use a single Sérsic profile in our fits, with the exception of objects that are clearly only moderately lensed (i.e., singly imaged with $\mu < 2$) and that show evidence of multiple source-plane components in the SMA imaging. This is true for J022016.5−060143 and J084933.4+021443.

Each SIE is fully described by the following five free parameters: the position of the lens relative to the SMA emission centroid ($\Delta\alpha_{\mathrm{lens}} = \alpha_{\mathrm{lens}} - \alpha_{880}$ and $\Delta\delta_{\mathrm{lens}} = \delta_{\mathrm{lens}} - \delta_{880}$; these can be compared with the position of the optical or near-IR counterpart relative to the SMA emission centroid: $\Delta\alpha_{\mathrm{NIR}} = \alpha_{\mathrm{NIR}} - \alpha_{880}$ and $\Delta\delta_{\mathrm{NIR}} = \delta_{\mathrm{NIR}} - \delta_{880}$), the mass of the lens (parameterized in terms of the angular Einstein radius, θ_{E}), the ellipticity of the lens (ϵ_{lens}; defined as $1 - b/a$), and the position angle of the lens (ϕ_{lens}; degrees east of north). When there is evidence for additional lenses from optical or near-IR imaging (see Figure 2), we estimate by-eye centroids for each lens (carrying an uncertainty of order 1 pixel, or $0\farcs04$ and $0\farcs12$ in the Keck-II/NIRC2-LGSAO and HST images, respectively) and fix the positions of the additional lenses with respect to the primary lens. Therefore, each additional lens has only 3 free parameters: θ_{E}, ϵ_{lens}, and ϕ_{lens}. We assume secondary, tertiary, etc., lenses are located at the same redshift as the primary lens, unless there is evidence against that assumption (e.g., J083051.0+013224).

Each Sérsic profile is fully described by the following seven free parameters: the position of the source relative to the primary lens ($\Delta\alpha_{\mathrm{s}} = \alpha_{\mathrm{s}} - \alpha_{\mathrm{lens}}$ and $\Delta\delta_{\mathrm{s}} = \delta_{\mathrm{s}} - \delta_{\mathrm{lens}}$), the intrinsic flux density (S_{in}), the Sérsic index (n_{s}), the half-light semi-major axis length (a_{s}), the ellipticity (ϵ_{s}, defined as $1 - b/a$), and the position angle (ϕ_{s}, degrees east of north).

The total number of free parameters for any given system is $N_{\mathrm{free}} = 5 + 3 \times (N_{\mathrm{lens}} - 1) + 7 * N_{\mathrm{source}}$, where N_{source} is the number of Sérsic profiles used.

We adopt loose, uniform priors for all model parameters. The 1-σ absolute astrometric solution between the SMA and optical/near-IR images is generally $0\farcs2$, so in our modeling efforts the prior on the position of the lens covers $\pm0\farcs6$ in both R.A. and Decl. (i.e., 3σ in each direction). In Section 3.2, we discuss the level of agreement between the astrometry from the images and the astrometry from the lens modeling. For θ_{E}, the prior covers $0\farcs1$–$6''$. The ellipticities of the lens and source are always restricted to be <0.7. No prior is placed on the position angle of the lens or source. The intrinsic flux density is allowed to vary from 0.1 mJy to the total flux density observed by the SMA. The source position is allowed to vary by $\pm1''$ relative to the position of the primary lens. The Sérsic index varies from 0.1 to 4.0. The half-light radius varies from $0\farcs05$ to $1\farcs5$.

For a given set of model parameters, GRAVLENS generates a surface brightness map of the lensed emission (note that no model of the emission from the lens is needed because the lenses are undetected in the SMA imaging). This surface brightness map can then be used as input to MIRIAD's UVMODEL task, which produces a "simulated visibility" dataset (V_{model}) by computing the Fourier transform of the model lensed image and sampling the resulting visibilities to match the sampling of the actual observed SMA visibility dataset (V_{SMA}). The quality of fit for a given set of model parameters is determined from the chi-squared value (χ^2) according to the following equations:

$$\chi^2 = \chi^2_{\mathrm{real}} + \chi^2_{\mathrm{imag}}, \quad (1)$$

$$\chi^2_{\mathrm{real}} = \sum_{u,v} \frac{[Re(V_{\mathrm{SMA}}(u,v)) - Re(V_{\mathrm{model}}(u,v))]^2}{\sigma^2_{\mathrm{real}}(u,v) + \sigma^2_{\mathrm{imag}}(u,v)}, \quad (2)$$

$$\chi^2_{\mathrm{imag}} = \sum_{u,v} \frac{[Im(V_{\mathrm{SMA}}(u,v)) - Im(V_{\mathrm{model}}(u,v))]^2}{\sigma^2_{\mathrm{real}}(u,v) + \sigma^2_{\mathrm{imag}}(u,v)}, \quad (3)$$

where $\sigma_{\mathrm{real}}(u,v) = \sigma_{\mathrm{imag}}(u,v)$ is the 1σ uncertainty level for each visibility and is determined from the system temperatures (this corresponds to a natural weighting scheme).

To sample the posterior probability density function (PDF) of our model parameters, we use EMCEE (Foreman-Mackey et al. 2013), a Markov chain Monte Carlo (MCMC) code that uses an affine-invariant ensemble sampler to obtain significant performance advantages over standard MCMC sampling methods (Goodman & Weare 2010).

We employ a "burn-in" phase with 250 walkers and 1000 iterations (i.e., 250,000 samplings of the posterior PDF) to identify the best-fit model parameters. This position is then used to initialize the "final" phase with 250 walkers and 20 iterations (i.e., 5,000 samplings of the posterior PDF) to determine uncertainties on the best-fit model parameters. The autocorrelation time for each parameter in a given ensemble of walkers and is of order unity for each parameter, implying that we have 5,000 independent samplings of the posterior PDF, more than enough to obtain a robust measurement of the mean and uncertainty on each parameter of the model.

During each MCMC iteration, we also measure the magnification factor at 880 μm, μ_{880} (we follow the nomenclature in the SMG literature here and use μ to refer to the total magnification obtained by summing over all individual lensed components). Here, we describe how we measure μ_{880}.

First, we take the unlensed, intrinsic source model and measure the total flux density (S_{in}) within an elliptical aperture (A_{in}) centered on the source with ellipticity and position angle equal to that of the source model and with a semi-major axis length of $2a_{\mathrm{s}}$. Second, we take the lensed image of the best-fit model and measure the total flux density (S_{out}) within the aperture A_{out}, where A_{out} is determined by using GRAVLENS to map A_{in} in the source plane to A_{out} in the image plane (using the lens parameters which correspond to the best-fit model). The magnification is then computed simply as $\mu_{880} = S_{\mathrm{out}}/S_{\mathrm{in}}$. The best-fit value and 1σ uncertainty are drawn from the posterior PDF, as with the other parameters of the model.

The choice of A_{in} has important implications for magnification measurements. For multiply imaged systems, apertures that are too large include in the source plane too much flux density that is far away from the caustic and relatively unmagnified. This is a particularly important issue for the models used here because the Sérsic index of the background source is a free parameter. The Sérsic index is partially degenerate with the half-light radius of the source, in the sense that good fits to the data can be obtained with a combination of small source size and small Sérsic index or large source size and large Sérsic index. In accordance with this, our model fits sometimes include relatively large sources where significant fractions of the unlensed flux density ($\approx10\%$–20%) arise from regions in the source plane far away from the caustic and hence contribute nothing to the observed lensed emission. This situation biases the estimate of μ_{880} below the true value. Conversely, apertures that are too small will omit flux density in the source plane that is detected at high significance in the SMA imaging, thus biasing the estimate of μ_{880} above the true value. Our choice—double the semi-major axis length of the source—represents a compromise between these two extremes.

3.2. Descriptions of Individual Objects

In this section, we describe the basic characteristics of each object in the SMA subsample, including the position of the lens relative to the SMA 880 μm emission centroid, the lensing configuration (where applicable), and any unique notes for each object. Figure 3 shows the best-fit model in comparison with the SMA data for every lensed SMG with a robust lens model. Tables 5 and 6 present, for lenses and sources respectively, the model parameter mean values and 1σ uncertainties as drawn from the posterior PDF for each parameter. Note that in some cases the posterior PDFs are non-Gaussian and therefore the best-fit model shown in Figure 3 does not always correspond perfectly to the model parameter mean values presented in Tables 5 and 6.

J021830.5−053124. SMA data from the compact and extended array configurations were originally presented in Ikarashi et al. (2011) and Wardlow et al. (2013). This paper presents new data obtained the in the very extended array, permitting the first resolved measurement of the 880 μm emission from this object. The best-fit lens model finds a position for the lens that is offset relative to that indicated in the *HST* image by 0.''26 in R.A. and −0.''11 in Decl. These values are near the expected level of 0.''2–0.''3 absolute astrometric uncertainty between the SMA and *HST* reference frames. The lensed emission is barely resolved by the SMA due to the small Einstein radius of the lens. The bulk of the source-plane emission originates outside the tangential caustic, favoring a two-image rather than four-image configuration (excluding the central demagnified image, which is never detected at the sensitivity levels probed in our data). This is consistent with the best-fit magnification factor of $\mu_{880} = 4.4 \pm 1.0$.

J022016.5−060143. This object is the subject of a detailed study by Fu et al. (2013). We present it here mostly for completeness, but also to test the validity of the model in Fu et al. (2013) using the visibility-plane lens modeling technique described in this paper. We use a two-component lens model and a three-component source model to reproduce the observed 880 μm emission. We enforce a minimum Einstein radius of $\theta_E > 0.''2$ for both lenses (corresponding to a minimum mass of $M_{\rm lens} > 1.6 \times 10^{10} M_{\odot}$). This is intended to reproduce the prior on the lens masses used by Fu et al. (2013) based on the lens stellar masses and an assumed relation between the stellar mass and dark matter halo mass. The best-fit parameters of this model are statistically consistent with those found by Fu et al. (2013), despite a very different approach in modeling the data. In particular, we find a modest magnification factor is appropriate for each of the three components, with an average total magnification factor of $\langle \mu_{880\,\mu{\rm m}} \rangle = 1.3 \pm 0.1$.

J083051.0+013224. The lensed emission has an unusual configuration that reflects the complexity of the foreground mass distribution due to the presence of a secondary lensing galaxy $<1''$ northwest of the primary lensing galaxy. WHT/ACAM spectroscopy shows that the primary lens is located at $z_{\rm lens} = 0.626$ based on *G*-band and Mg absorption features, while the secondary lens has very faint continuum and an emission line at observed frame 7462 Å. If this feature is [O II]3727, then its redshift is $z_{\rm lens2} = 1.002$. The best-fit lens model for this system assigns each of the foreground galaxies approximately equal Einstein radii ($\approx$0.''4). Given the stated lens and source redshifts, this implies lens masses of $\approx 0.7 \times 10^{11} M_{\odot}$ and $1.6 \times 10^{11} M_{\odot}$, respectively.

J084933.4+021443. This object is the subject of a detailed study by Ivison et al. (2013). It is presented here for complete-

ness and to ensure that the use of a visibility-plane lens model provides the same results as given in Ivison et al. (2013). Note that the center and extent of the image cutout shown in Figure 3 has been adjusted from the SMA emission centroid used in Figure 2 to include only the lens and the lensed source (dubbed "T" in Ivison et al. 2013). This is done simply to facilitate the comparison of model and data. An additional two sources used in the fitting process are not shown in this diagram. These two unlensed sources are modeled using the same visibility method but assuming no magnification by foreground objects. We find evidence for a larger magnification factor for "T" than Ivison et al. (2013): $\mu_{880} = 2.8 \pm 0.2$ instead of $\mu_{880} = 1.5 \pm 0.2$. A 2σ emission peak located just northwest of the lens can be seen in Figure 3. If real, this emission peak supports the notion of a higher magnification factor for this object. Overall, however, our results are in broad agreement with those of Ivison et al. (2013).

J085358.9+015537. Although the image separations are small for this object ($\theta_E = 0.''553 \pm 0.''004$), the S/N is high. The source appears to lie very close to the caustic (which is itself small due to the low ellipticity of the lens), implying a high magnification factor $\mu_{880} = 15.3 \pm 3.5$.

J090302.9−014127. The image separations are close to the smallest values found in the SMA subsample ($\theta_E = 0.''35 \pm 0.''02$). There has been tentative evidence (3σ) of CO($J = 5$–4) emission from the lens at $z_{\rm lens} = 0.942 \pm 0.004$ (Lupu et al. 2012), but this has not been confirmed with subsequent, more sensitive observations that rule out lens redshifts from 0.922 to 0.944 (Omont et al. 2011). In the lens model presented here, the lens is assumed to be an insignificant submm emitter.

J090311.6+003906. Because of the high S/N and well-separated images of the background source ($\theta_E = 1.''52 \pm 0.''03$), the lens model is well-constrained for this object. However, the image of the residual visibilities shows emission at the ±3σ level, possibly an indication of complexity in the source structure that is not captured by a single Sérsic profile.

J090740.0−004200. The counter image to the northwest of the lens is detected at the 4σ level and provides good constraints on the lens model for this object.

J091043.1−000321. This is one of a handful of objects with emission at the $> \pm 2\sigma$ level that can be seen in the surface brightness map made from the residual visibilities. An edge-on galaxy located 4.''4 to the northwest with a position angle of 135° east of north could be responsible for an external shear that has not been included in the lens model. Alternatively, the residual flux density may reflect a more complicated source structure than can be represented by our choice of a single Sérsic profile.

J091305.0−005343. The best-fit lens models for this object are obtained when the source is relatively large and most of it is located outside the region in the source plane that produces multiple images. For this reason, the best-fit magnification factor is relatively low ($\mu_{880} = 2.1 \pm 0.3$).

J091840.8+023047. This object is unique in having no counterpart within $1''$ of the 880 μm centroid in the *HST*/F110W Snapshot imaging. There is no obvious morphological signature of lensing based on the SMA data, so this may be a rare unlensed SMG. It is not included in Figure 3 since no lens model is available. Further investigation is needed to determine the nature of this object.

J103826.6+581542. This object was originally presented by Wardlow et al. (2013). We present it here for completeness and to test the validity of the model in Wardlow et al. (2013)
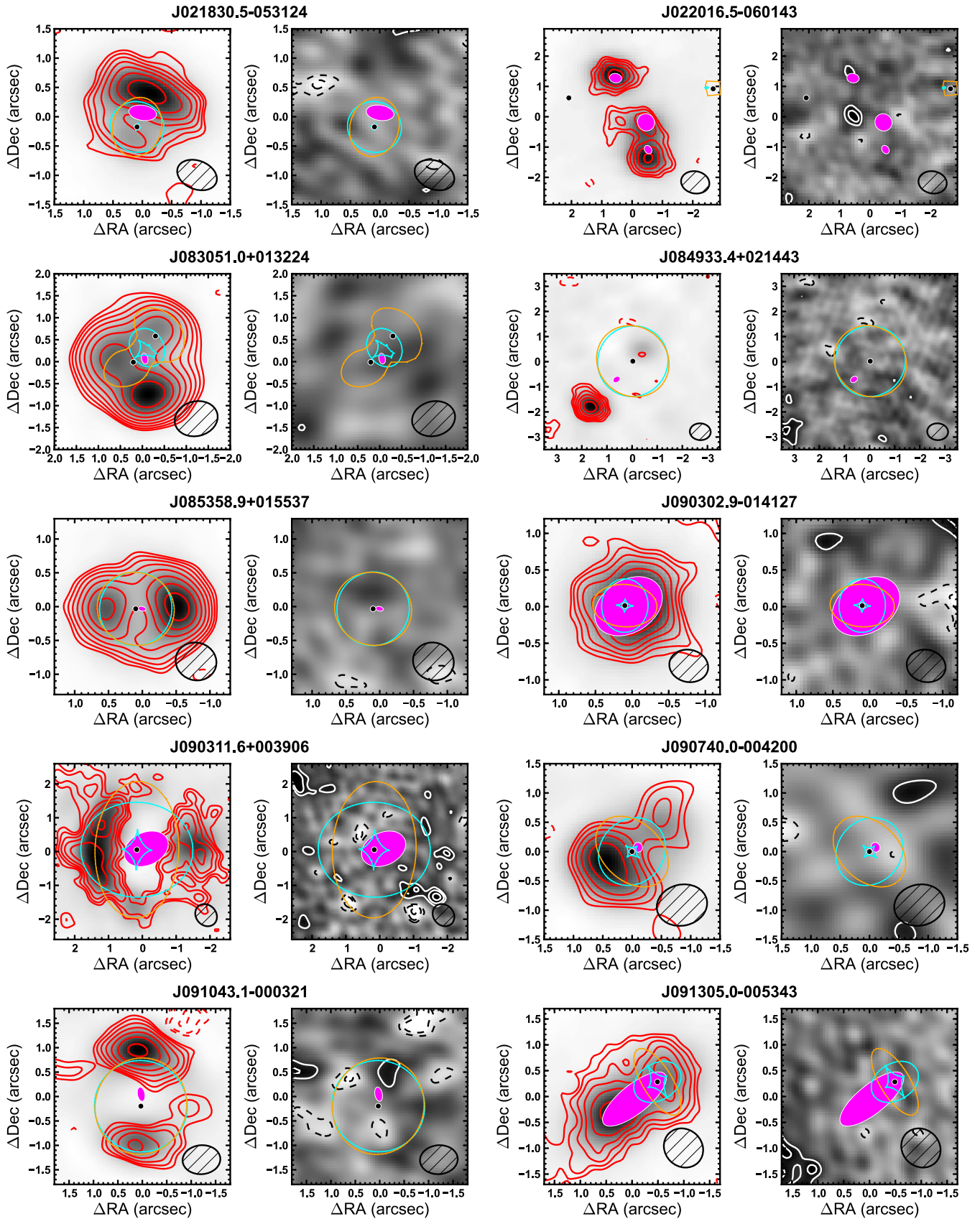
Figure 3. Comparison of best-fit lens models with SMA data. Odd columns show the surface brightness maps of the best-fit model lensed emission (grayscale) in comparison with the observed surface brightness maps from the SMA (red contours, beginning at $\pm 2\sigma$ and increasing by factors of $\sqrt{2}$). Even columns show the residual surface brightness maps obtained by subtracting the best-fit lens model visibilities with the observed visibilities by the SMA (contours drawn at same levels as odd panels). For reference, all panels show the critical curves (orange line), caustics (cyan lines), position of the lens(es) (black circles), the half-light area of the background source(s) (magenta filled ellipses), and the FWHM of the SMA synthesized beam (black hatched ellipses).

(A color version of this figure is available in the online journal.)
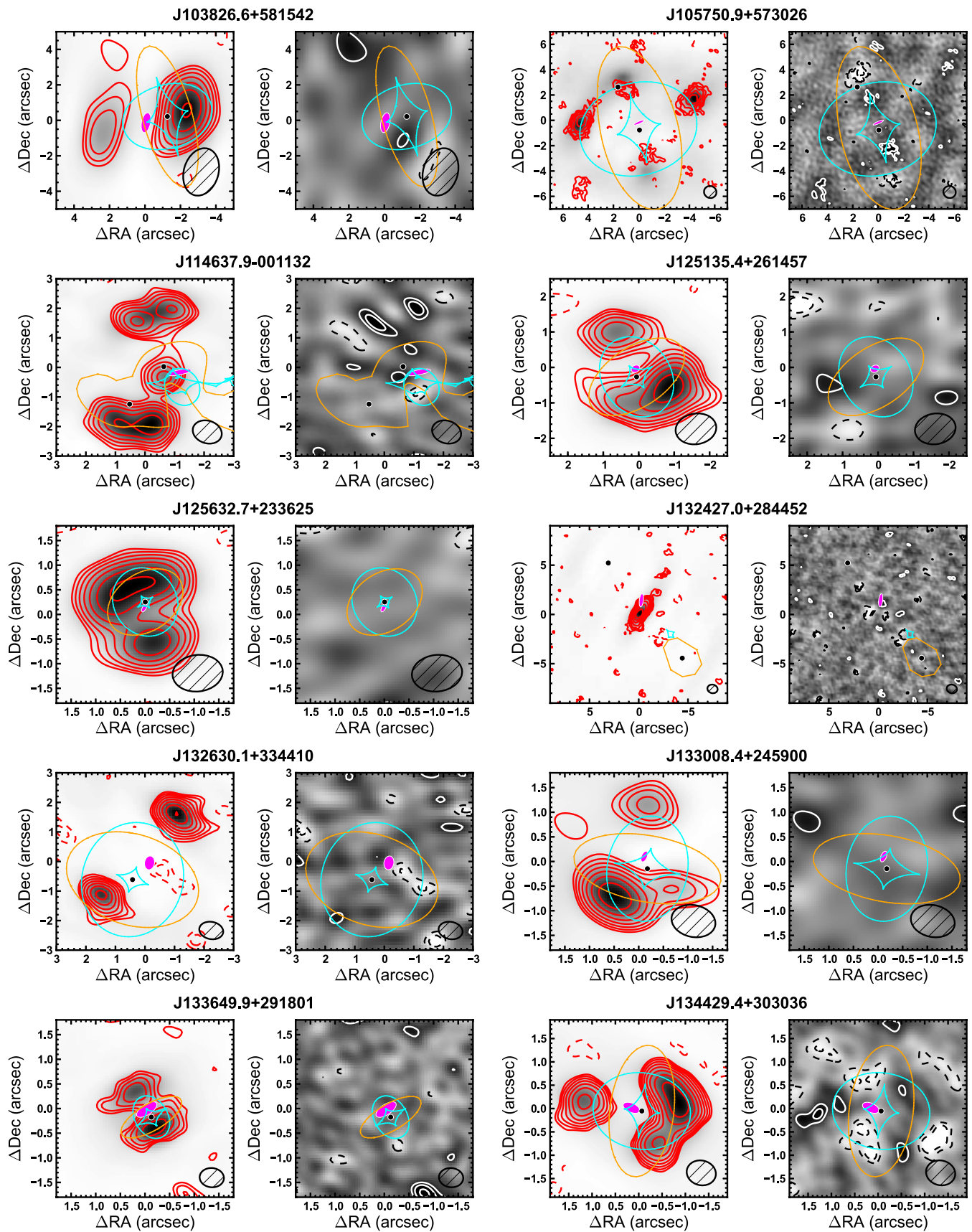
Figure 3. (Continued)
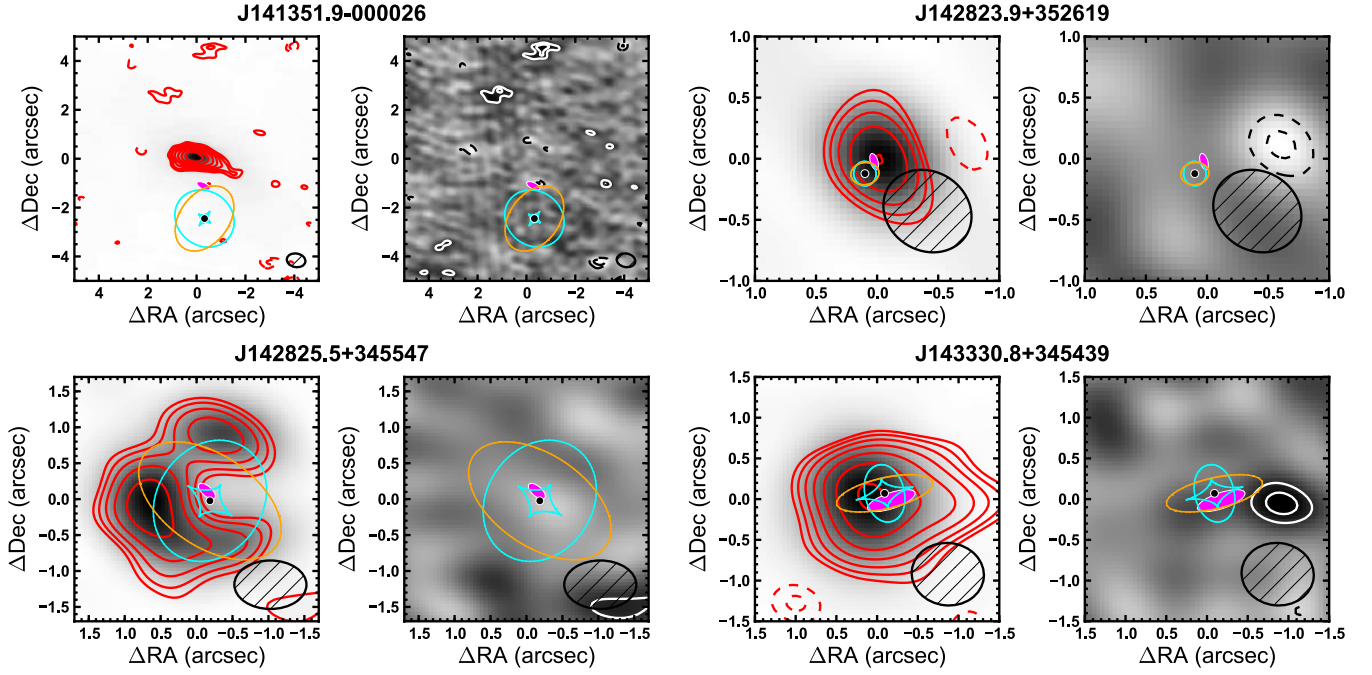
Figure 3. (Continued)

Table 5
Gravitational Lens Model Results: Lens Properties

Object	$\Delta\alpha_{\rm NIR}$ ($''$)	$\Delta\delta_{\rm NIR}$ ($''$)	$\Delta\alpha_{\rm lens}$ ($''$)	$\Delta\delta_{\rm lens}$ ($''$)	$\theta_{\rm E}$ ($''$)	$\epsilon_{\rm lens}$	$\phi_{\rm lens}$ (deg)	χ^2	$N_{\rm DOF}$
J021830.5−053124	−0.17	−0.02	0.09 ± 0.04	−0.13 ± 0.05	0.44 ± 0.02	0.35 ± 0.10	156 ± 18	106027.4	114284
J022016.5−060143	2.1	0.6	2.07 ± 0.01	0.63 ± 0.01	0.27 ± 0.13	0.29 ± 0.13	114 ± 52	131464.2	133819
. . .	−4.76	0.3	−4.76	0.3	0.34 ± 0.14	0.30 ± 0.18	53 ± 54	. . .	. . .
J083051.0+013224	0.18	0.10	0.20 ± 0.01	0.00 ± 0.02	0.39 ± 0.02	0.43 ± 0.05	123 ± 3	97761.3	100561
. . .	0.54	0.595	0.54	0.595	0.43 ± 0.02	0.25 ± 0.07	47 ± 9	. . .	. . .
J084933.4+021443	−7.90	−0.60	−7.90	−0.60	1.41 ± 0.04	0.11 ± 0.06	62 ± 22	188965.5	168376
J085358.9+015537	0.04	0.02	0.09 ± 0.03	−0.03 ± 0.01	0.553 ± 0.004	0.06 ± 0.02	70 ± 12	160445.4	161200
J090302.9−014127	0.20	0.16	0.092 ± 0.006	0.03 ± 0.02	0.33 ± 0.02	0.39 ± 0.07	83 ± 5	124529.4	124378
J090311.6+003906	0.07	0.10	0.13 ± 0.02	0.03 ± 0.05	1.52 ± 0.03	0.34 ± 0.05	179 ± 4	198305.2	188164
J090740.0−004200	−0.03	0.17	0.01 ± 0.04	0.03 ± 0.04	0.59 ± 0.04	0.50 ± 0.08	44 ± 5	98244.2	91314
J091043.1−000321	0.22	−0.14	0.05 ± 0.02	−0.18 ± 0.01	0.95 ± 0.02	0.08 ± 0.03	152 ± 24	171966.9	159664
J091305.0−005343	−0.32	0.35	−0.45 ± 0.05	0.38 ± 0.08	0.43 ± 0.07	0.51 ± 0.13	43 ± 14	211928.5	200412
J103826.6+581542	−1.80	0.25	−1.1 ± 0.2	0.27 ± 0.09	2.0 ± 0.2	0.54 ± 0.11	18 ± 3	78239.2	76704
J105750.9+573026	−0.65	−1.19	−0.11 ± 0.05	−0.80 ± 0.08	3.86 ± 0.01	0.52 ± 0.01	14 ± 1	142740.4	120764
. . .	1.7	3.4	1.7	3.4	0.12 ± 0.01	0.54 ± 0.11	170 ± 9	. . .	. . .
J114637.9−001132	−0.40	0.02	−0.59 ± 0.02	0.02 ± 0.02	0.65 ± 0.02	0.26 ± 0.04	114 ± 19	90621.1	94863
. . .	1.154	1.270	1.154	1.270	0.67 ± 0.01	0.50 ± 0.04	68 ± 2	. . .	. . .
. . .	−3.076	−1.688	−3.076	−1.688	0.61 ± 0.03	0.33 ± 0.07	95 ± 12	. . .	. . .
. . .	−4.340	0.632	−4.340	0.632	0.51 ± 0.04	0.50 ± 0.10	77 ± 6	. . .	. . .
J125135.4+261457	0.04	0.13	0.05 ± 0.04	−0.25 ± 0.09	1.02 ± 0.03	0.46 ± 0.06	122 ± 1	72453.5	62912
J125632.7+233625	0.11	0.25	0.00 ± 0.01	0.25 ± 0.01	0.68 ± 0.01	0.31 ± 0.03	123 ± 1	62465.3	45880
J132427.0+284452	3.09	5.22	3.09	5.22	1.7 ± 0.4	0.34 ± 0.14	81 ± 16	228617.0	213957
. . .	−7.51	−9.66	−7.51	−9.66	2.2 ± 0.3	0.14 ± 0.09	88 ± 15	. . .	. . .
J132630.1+334410	0.68	−0.78	0.53 ± 0.05	−0.54 ± 0.05	1.80 ± 0.02	0.26 ± 0.04	66 ± 4	43605.2	38964
J133008.4+245900	−0.24	−0.02	−0.14 ± 0.03	−0.13 ± 0.02	0.88 ± 0.02	0.52 ± 0.03	81 ± 1	71948.3	52744
J133649.9+291801	. . .	. . .	0.00 ± 0.11	0.03 ± 0.16	0.40 ± 0.03	0.38 ± 0.14	120 ± 13	100742.9	95844
J134429.4+303036	−0.03	−0.10	−0.03 ± 0.02	−0.01 ± 0.02	0.92 ± 0.02	0.39 ± 0.06	172 ± 14	182936.2	171864
J141351.9−000026	−0.32	−2.65	−0.32 ± 0.03	−2.50 ± 0.03	1.13 ± 0.09	0.31 ± 0.12	118 ± 33	132668.6	123420
J142413.9+022303	−0.11	0.79	−0.27 ± 0.03	0.63 ± 0.03	0.57 ± 0.01	0.29 ± 0.01	62 ± 1	108899.5	144191
. . .	0.025	−0.327	0.025	−0.327	0.40 ± 0.01	0.06 ± 0.02	133 ± 14	. . .	. . .
J142823.9+352619	−0.14	−0.02	−0.01 ± 0.10	0.00 ± 0.11	0.10 ± 0.03	0.36 ± 0.18	87 ± 40	17284.0	17036
J142825.5+345547	0.25	−0.05	−0.20 ± 0.03	−0.04 ± 0.03	0.77 ± 0.03	0.46 ± 0.06	56 ± 5	93163.7	75448
J143330.8+345439	0.00	0.05	−0.07 ± 0.03	0.07 ± 0.02	0.28 ± 0.02	0.59 ± 0.08	104 ± 7	91554.9	117732

Table 6
Gravitational Lens Model Results: Source Properties

IAU Name	$\Delta\alpha_s$ (″)	$\Delta\delta_s$ (″)	n_s	a_s (″)	ϵ_s	ϕ_s (deg)	$\mu_{880\,\mu m}$
J021830.5−053124	−0.08 ± 0.03	0.22 ± 0.04	2.1 ± 0.9	0.33 ± 0.12	0.29 ± 0.13	82 ± 22	4.4 ± 1.0
J022016.5−060143	−1.54 ± 0.02	0.65 ± 0.02	2.1 ± 0.8	0.16 ± 0.05	0.25 ± 0.10	68 ± 34	1.5 ± 0.3
...	−2.56 ± 0.02	−0.82 ± 0.07	1.7 ± 0.8	0.30 ± 0.07	0.40 ± 0.13	45 ± 53	1.2 ± 0.1
...	−2.61 ± 0.02	−2.05 ± 0.02	1.4 ± 0.7	0.28 ± 0.06	0.19 ± 0.09	72 ± 44	1.2 ± 0.0
J083051.0+013224	−0.25 ± 0.01	0.08 ± 0.02	1.8 ± 0.5	0.14 ± 0.01	0.32 ± 0.06	20 ± 7	6.9 ± 0.6
J084933.4+021443	0.67 ± 0.03	−0.73 ± 0.03	2.1 ± 0.7	0.15 ± 0.03	0.20 ± 0.12	103 ± 35	2.8 ± 0.2
...	11.3	3.0	0.4 ± 0.3	0.25 ± 0.02	0.33 ± 0.10	24 ± 18	1.0
...	14.3	4.0	2.0 ± 0.9	0.17 ± 0.07	0.43 ± 0.17	93 ± 34	1.0
J085358.9+015537	−0.09 ± 0.03	0.001 ± 0.002	2.0 ± 0.7	0.06 ± 0.01	0.33 ± 0.14	83 ± 17	15.3 ± 3.5
J090302.9−014127	−0.06 ± 0.01	−0.01 ± 0.01	2.5 ± 0.6	0.42 ± 0.12	0.22 ± 0.12	116 ± 23	4.9 ± 0.7
J090311.6+003906	−0.26 ± 0.03	0.04 ± 0.05	2.2 ± 0.4	0.52 ± 0.10	0.35 ± 0.06	94 ± 11	11.1 ± 1.1
J090740.0−004200	−0.15 ± 0.03	0.14 ± 0.03	2.0 ± 1.1	0.16 ± 0.10	0.31 ± 0.14	73 ± 57	8.8 ± 2.2
J091043.1−000321	−0.017 ± 0.008	0.23 ± 0.02	1.5 ± 0.5	0.13 ± 0.02	0.35 ± 0.12	5 ± 20	10.9 ± 1.3
J091305.0−005343	0.42 ± 0.05	−0.37 ± 0.06	3.0 ± 0.6	0.76 ± 0.12	0.56 ± 0.13	129 ± 10	2.1 ± 0.3
J103826.6+581542	1.1 ± 0.2	−0.33 ± 0.06	3.0 ± 0.7	0.45 ± 0.18	0.44 ± 0.19	129 ± 32	7.1 ± 1.5
J105750.9+573026	−0.07 ± 0.04	0.76 ± 0.06	2.4 ± 0.8	0.57 ± 0.08	0.58 ± 0.11	122 ± 6	9.2 ± 0.4
J114637.9−001132	−0.50 ± 0.06	−0.28 ± 0.04	0.5[a]	0.38 ± 0.03	0.77 ± 0.03	107 ± 4	9.5 ± 0.6
J125135.4+261457	0.02 ± 0.04	0.22 ± 0.09	1.9 ± 0.6	0.15 ± 0.03	0.22 ± 0.10	109 ± 32	11.0 ± 1.0
J125632.7+233625	0.014 ± 0.006	−0.12 ± 0.01	1.1 ± 0.6	0.07 ± 0.01	0.37 ± 0.14	140 ± 21	11.3 ± 1.7
J132427.0+284452	−3.8 ± 0.4	−5.1 ± 0.6	2.4 ± 0.4	0.72 ± 0.09	0.69 ± 0.01	169 ± 17	2.8 ± 0.4
J132630.1+334410	−0.60 ± 0.03	0.60 ± 0.03	1.1 ± 0.3	0.22 ± 0.02	0.18 ± 0.09	150 ± 15	4.1 ± 0.3
J133008.4+245900	0.05 ± 0.01	0.23 ± 0.02	1.6 ± 0.7	0.09 ± 0.03	0.37 ± 0.10	129 ± 29	13.0 ± 1.5
J133649.9+291801	−0.04 ± 0.09	−0.05 ± 0.15	1.2 ± 0.5	0.19 ± 0.03	0.43 ± 0.12	125 ± 13	4.4 ± 0.8
J134429.4+303036	0.22 ± 0.02	0.04 ± 0.02	1.9 ± 0.5	0.24 ± 0.06	0.39 ± 0.07	100 ± 15	11.7 ± 0.9
J141351.9−000026	0.13 ± 0.13	1.40 ± 0.09	1.5 ± 0.5	0.30 ± 0.04	0.48 ± 0.12	62 ± 7	1.8 ± 0.3
J142413.9+022303	−0.24 ± 0.03	−0.53 ± 0.03	2.9 ± 0.3	0.64 ± 0.07	0.27 ± 0.09	77 ± 12	4.6 ± 0.5
J142823.9+352619	−0.00 ± 0.07	0.03 ± 0.08	1.9 ± 1.2	0.10 ± 0.07	0.33 ± 0.18	64 ± 62	3.0 ± 1.5
J142825.5+345547	0.05 ± 0.01	0.15 ± 0.03	0.7 ± 0.4	0.16 ± 0.04	0.50 ± 0.09	49 ± 10	10.3 ± 1.7
J143330.8+345439	−0.08 ± 0.02	−0.07 ± 0.02	1.9 ± 0.7	0.31 ± 0.06	0.55 ± 0.14	116 ± 13	4.5 ± 0.4

Note. [a] $n_s = 0.5$ was assumed for this source.

using the visibility-plane lens modeling technique described in this paper. Our results for the size (0″.45 ± 0″.18 versus <0″.5) and magnification factor of the background source (7.1 ± 1.5 versus $5.32^{+1.28}_{-1.06}$) are consistent with those reported in Wardlow et al. (2013). Since a redshift measurement for the background source remains unavailable, no further analysis is possible for this object.

J105712.2+565457. This object was originally presented by Wardlow et al. (2013). We present a slightly modified reduction of this object here. Instead of MIRIAD's MOSSDI task, which was used in Wardlow et al. (2013) to image this object, here we have shifted all of the visibility datasets to have the same phase center and then used MIRIAD's CLEAN task. This resulted in slightly improved spatial resolution (0″.68 × 0″.57 versus 1″.18 × 0″.97), that is still not sufficient to distinguish cleanly separated images from a single lensed source. It is not included in Figure 3 since no lens model is available. Further investigation is needed to determine the nature of this object.

J105750.9+573026. This object was originally analyzed in a series of papers reporting its discovery, interstellar medium (ISM) properties, gas dynamics, and (on the basis of K_p-band imaging) lensing geometry (Conley et al. 2011; Scott et al. 2011; Riechers et al. 2011b; Gavazzi et al. 2011). We present new very extended array data here and compare the SMA and Keck lens models. The very extended array data are not as sensitive as the compact array data, so natural weighting provides a beam size of 0″.99 × 0″.94. This is insufficient to resolve the individual images of the lensed source seen in the image from the compact array only data and is further indication that the lens model is primarily constrained by the compact array data. Because the S/N and spatial resolution in the Keck image are superior to those of the SMA image, we fix the parameters of the lens to match those of the model found by Gavazzi et al. (2011). We find a similar magnification factor at 880 μm compared to K_p (9.2 ± 0.4 versus 10.9 ± 0.7). The model has difficulty reproducing the locations of the images seen in the SMA data. In addition, we find an offset in the position of the lens of 0″.54 in R.A. and 0″.4 in Decl. This represents a ≈2–3σ discrepancy in R.A. and may be an indication that some of the assumptions in our model are over-simplifications.

J113526.3−014605. There is no counterpart detected in a 15-minute K_s integration with the WHT. The SMA 880 μm image is clearly resolved, but does not show individual, well-separated images of a lensed SMG. It is not included in Figure 3 since no lens model is available. Further investigation is required to determine whether strong lensing is occurring in this object. The main avenues for progress are higher-spatial resolution submm imaging (e.g., SMA very extended array) and deeper observations in the optical or near-IR to determine whether or not there is a lensing galaxy.

J114637.9−001132. This object was originally presented by Fu et al. (2012). Here, we present new SMA extended array data that resolve the lensed emission into five striking images of the SMG. The position and morphology of the lensed SMG in the source plane reported here are statistically consistent with those found by Fu et al. (2012). The presence of flux density at the 3σ level in the map of the residual visibilities (see Figure 3) indicates our simple assumptions about

the lens mass model (singular isothermal ellipsoids at the locations of galaxies identified in the Keck-II/NIRC2-LGSAO and *HST*/F110W imaging) and/or the background source Sérsic profile may be breaking down.

J125135.4+261457. The offset between the position of the lens from the lens model and from the WHT astrometry is $0\rlap{.}''01$ in R.A. and $0\rlap{.}''38$ in Decl. compared to the best-fit parameters from the lens model. The offset in Decl. is larger than expected given the astrometric uncertainty in aligning the SMA and WHT reference frames. On the other hand, the lens model correctly predicts the ellipticity and position angle of the lens potential (no priors were assumed for the shape of the lens potential), a strong indication that the lens model is robust.

J125632.7+233625. The S/N is very high in this object and the images of the lensed SMG are well-separated, making the parameters of the lens model very robust.

J132427.0+284452. This object is the subject of detailed studies by (George et al. 2013) and H. Fu et al. (in preparation) to explore its dust, gas, and stellar properties. In this paper, we use the Keck-II/NIRC2-LGSAO image to constrain the positions of the lenses and apply our visibility-plane lens modeling technique to the SMA data. We find that a two-lens mass model is needed to reproduce the observed data. These correspond directly to two galaxies detected at high significance in the Keck imaging. However, it should be noted that there are two nearby clusters detected in the Red-Sequence Cluster (RSC) survey (RCS J132427+2845.2 at $z = 0.997 \pm 0.017$ and RCS J132419+2844.7 at $z = 0.802 \pm 0.018$ Gladders & Yee 2005). The centers of these clusters are uncertain due to a lack of X-ray data and no clear brightest-cluster galaxy, but the RCS surface density map suggests that RCS J132427+2845.2 lies only $10''$ away from lensed SMG. Our lens modeling here does not account for the presence of this cluster. Furthermore, the background source is not multiply imaged in the SMA data, so the constraints on the lens parameters are weak. The possibility of counter images falling outside of the SMA primary beam (FWHM of $36''$ at $880\,\mu\mathrm{m}$) is low due to the lack of such a counterpart in the SPIRE maps.

J132630.1+334410. Two well-separated images of the lensed SMG are obvious in the SMA data, indicating the source is strongly lensed but is not among the highest magnification sources. The lens modeling result is consistent with this ($\mu_{880} = 4.1 \pm 0.3$), suggesting a robust model fit.

J132859.3+292317. The nature of this object is unclear based on existing data. It is well-detected and clearly spatially resolved by the SMA at $880\,\mu\mathrm{m}$. The problem is the lack of optical or near-IR imaging at a depth beyond what is achieved in SDSS, where the object is undetected in all bands. One plausible interpretation is that the object is lensed by a relatively low-mass foreground galaxy at intermediate redshift so that it is undetected in the SDSS images. Alternatively, it is conceivable that the object is not lensed and has an intrinsic submm flux density of $S_{880} = 51.8 \pm 2.0$ mJy. We consider this latter option unlikely since there are no known SMGs with intrinsic submm flux densities that high. However, without additional data to confirm this intuition, we do not consider this object further in our analysis. It is not included in Figure 3 since no lens model is available.

J133008.4+245900. Multiple, well-separated images are detected in the SMA data, consistent with the relatively large inferred magnification factor from the lens model ($\mu_{880} = 13.0 \pm 1.5$), suggesting a robust lens model has been obtained.

J133649.9+291801. This object is similar to J132859.3+292317 in that there is no significant detection in any of the SDSS optical bands, nor is deeper optical or near-IR imaging available. However, the SMA morphology provides evidence typical of strong lensing. Here, we assume that the object is strongly lensed.

J134429.4+303036. The lensed images are well-separated and well-detected in the SMA data. In fact, the S/N is so high that the map of the residual visibilities reveals emission at the $\pm 3\sigma$ level, likely indicating that some of our model assumptions are over-simplifications. Nevertheless, the model captures the vast majority of the SMA emission and therefore provides a fair representation of intrinsic source size and luminosity. This object is similar to J125135.4+261457 in that the lens model successfully predicts the ellipticity and position angle of the lens potential without any non-standard priors placed on these parameters.

J141351.9−000026. No counter image of this target is detected in the SMA data, an immediate indication that this object is not strongly lensed. The possibility of counter images falling outside of the SMA primary beam (FWHM of $36''$ at $880\,\mu\mathrm{m}$) is low due to the lack of such a counterpart in the SPIRE maps. The lens modeling confirms this, with $\mu_{880} = 1.8 \pm 0.3$. The lens is located $7\rlap{.}''7$ northeast of a brightest cluster galaxy (BCG). The lens redshift used here is from the BCG, and in order to derive the mass of the lens from its θ_E value, we have assumed that it is located at the same redshift as the BCG.

J142413.9+022303. This object is the subject of a detailed study by Bussmann et al. (2012). We do not reproduce the results of the previous work here because it used the same visibility-plane lens modeling technique outlined in this paper.

J142823.9+352619. This object was originally discovered in *Spitzer* mid-IR imaging of the Boötes Field (Borys et al. 2006) and has since been the subject of a great many follow-up observations, a thorough summary of which may be found in Wardlow et al. (2013). We present new SMA extended array data which do not resolve the source, further corroborating the idea that this object is very small and is not strongly lensed (i.e., $\mu < 2$). Since we know that there is an intervening galaxy along the line of sight to the *Herschel* source, we impose a minimum Einstein radius for the lens of $\theta_E > 0\rlap{.}''1$ (corresponding to a minimum lens mass of $M_{\mathrm{lens}} > 10^{10}\,M_\odot$). The constraints on the lens model are weak. One of the few robust claims we can make regarding this source is that it is very small ($a_s < 0\rlap{.}''2$).

J142825.5+345547. This object is the subject of a detailed study by J. L. Wardlow et al. (in preparation). The lens model suggests the lens is located $0\rlap{.}''20$ west of the SMA emission centroid, but the peak of the edge-on spiral seen in the astrometrically-aligned *HST* image occurs $0\rlap{.}''25$ east of the SMA emission centroid. This is a difference of $0\rlap{.}''45$ in R.A. (the difference in Decl. is insignificant) and is larger than the expected 1σ astrometric uncertainty of $0\rlap{.}''2$. However, estimating the peak position of the lensing galaxy is difficult because it is nearly exactly edge-on with a prominent dust lane and very little bulge. Moreover, the lensed images are well-resolved and well-detected in the SMA data, and the lens model correctly predicts the position angle and approximate ellipticity of the lens without any priors on these parameters. For these reasons, we consider the lens model for this object to be robust.

J143330.8+345439. This object was originally presented in Wardlow et al. (2013). We present a slightly modified reduction of this object here in which we shift all of the visibility datasets to have the same phase center and then use MIRIAD's
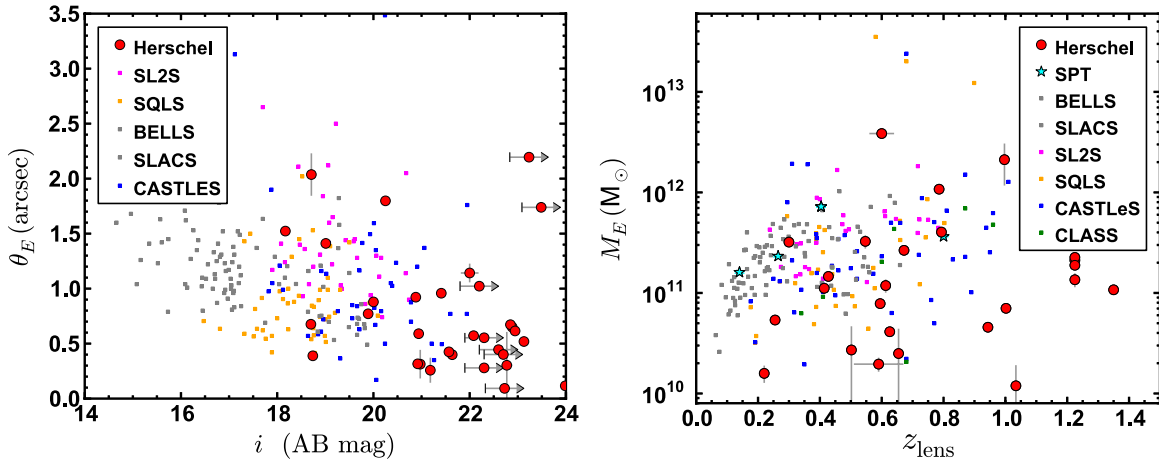
Figure 4. Properties of lenses discovered by *Herschel* (red circles) and SPT (cyan stars), compared with a compilation of lenses from BELLS and SLACS (gray squares), SL2S (magenta squares), CASTLES (blue squares), CLASS (green squares), and SQLS (yellow squares). Left: Einstein radius (θ_E) as a function of i-band AB magnitude. The *Herschel* sample is fainter and shows a wider range in θ_E values than any of the previous samples of lenses. Right: mass enclosed within θ_E as a function of lens redshift. *Herschel* has identified lenses that are lower in mass or higher in redshift than any of the optically-based searches (SLACS, BELLS, and SL2S). The range in parameter space occupied by the *Herschel* data points is comparable to that of CASTLES, CLASS, and SQLS, but *Herschel* promises to provide a sample size that is over an order of magnitude larger (González-Nuevo et al. 2012).

(A color version of this figure is available in the online journal.)

CLEAN task. This provides slightly improved spatial resolution that is still insufficient to identify clearly separated images of a single lensed source. Nevertheless, we use the knowledge that spectroscopic redshifts are available for both the lens and background source to infer that strong lensing is occurring. We then model this object using the same set of model parameters as applied to the other objects in the SMA subsample. Note that absolute astrometric calibration based on alignment to existing ground-based imaging is not available in the *HST* image for this object, but the lens model still finds a position for the lens that is in reasonable agreement (within $0\farcs4$) with that in the *HST* image.

J144556.1−004853. No lens or source redshift is available for this object. The SMA data resolve the $880\,\mu$m emission, but detect the source at relatively low S/N (S/N < 6). Keck-II/NIRC2-LGSAO K_s-band imaging detects a counterpart that is located between the resolved components identified in the SMA data. This could be a detection of the lens, or it could simply be an intrinsic component of an unlensed SMG. Unlike J132859.3+292317, the total $880\,\mu$m flux density ($S_{880} = 9.0 \pm 2.1$ mJy) is not unprecedented for unlensed SMGs. It is not included in Figure 3 since no lens model is available. Further investigation is required to determine if strong lensing is occurring in this object.

4. PROPERTIES OF LENSES DISCOVERED BY *HERSCHEL*

Two of the most basic properties of strong gravitational lensing galaxies are their i-band magnitudes (tracing the stellar light emitted by the lens, since the background sources detected by *Herschel* are dust-obscured and high-redshift, and therefore faint in the optical) and Einstein radii. The left panel of Figure 4 shows these values for the objects in the SMA subsample with robust lens models and compares them to other strong lenses found in SLACS (Bolton et al. 2008), BELLS (Brownstein et al. 2012), CASTLeS (Muñoz et al. 1998), and CLASS (Myers et al. 2003; Browne et al. 2003).

In this figure, the i-band magnitudes for the SMA subsample come from SDSS DR9 (see Section 2.7 for details). We account

for multiple lens systems by assigning a fraction of the total SDSS i-band flux density to each lens. The appropriate fraction is determined from the ratio of the θ_E for that lens to the sum of the θ_E values for that system. This explains why a few objects appear in the left panel of Figure 4 to have i-band magnitudes below the SDSS limit of $i \approx 22.5$ (AB mag).

Figure 4 helps clarify the observational distinctions between lenses discovered via wide-field (sub)mm surveys (i.e., *Herschel* and SPT) and optically-selected surveys like SLACS, BELLS, SL2S, and SQLS. Note that the CASTLeS and CLASS samples of lenses have similar properties to the *Herschel* and SPT lenses, but will not grow further in size. Although BELLS and SL2S go much deeper in the i-band than SLACS, they are still biased toward brighter lenses than the source-selected surveys by the need for detections in SDSS optical spectroscopy. Even SQLS, which does not require optical spectroscopic detections from SDSS, has lenses with brighter i-band magnitudes than the source-selected samples. Indeed, 10 out of 30 objects in the SMA subsample are undetected in SDSS imaging, likely indicating that the SMA subsample probes higher redshifts or lower lens masses than any of the previous surveys. There is very little overlap in the observational properties of *Herschel*-selected lenses and SLACS or BELLS lenses, indicating that the two techniques are highly complementary.

With only a modest investment of observing time ($\approx$1 hr on-source per target) with 4–6 m class optical telescopes, it is possible to measure spectroscopic redshifts for most of the lenses in the SMA subsample (see Sections 2.3 and 2.4 for details). We use the standard equations from Schneider et al. (1992) to compute the mass inside θ_E for the lensing galaxies, M_E. These values are shown for the SMA subsample as a function of lens redshift, z_{lens}, in the right panel of Figure 4. This plot emphasizes the new range in parameter space that is probed by *Herschel*-selected lenses compared to SDSS-based lens searches: high redshift ($z_{lens} > 0.6$) and low mass ($M_E < 10^{11}\,M_\odot$). The distinction in redshift confirms the evidence based on photometric redshifts presented by González-Nuevo et al. (2012). The objects from the literature with the most overlap with the SMA subsample are those from CASTLeS, CLASS, and SQLS—as expected, since these are

18

source-selected samples of lenses. It should be noted that this comparison is not entirely fair to the *Herschel*-selected lenses because the SMA subsample is missing lens redshifts for optically-faint targets that are likely to have lower mass or lie at higher redshift ($z_{lens} \gtrsim 1$). A handful of lenses identified by the SPT (Hezaveh et al. 2013) are also shown in this diagram, and are likely to have ensemble properties similar to those of the *Herschel*-selected lenses once statistically significant sample sizes are available.

Lenses discovered by *Herschel* have relatively high ellipticities compared to lenses selected from optical surveys. We measure a median ellipticity of $\epsilon_{lens} = 0.35 \pm 0.15$. In comparison, Brewer et al. (2012) study a subset of the SLACS sample where the foreground deflector has an inclined disk and measure a median ellipticity of $\epsilon_{lens} = 0.39 \pm 0.07$. There is a theoretical basis for why such an effect could occur: optical surveys for lenses might miss a large segment of highly inclined lenses due to dust obscuration by the foreground deflector (e.g., Bartelmann & Loeb 1998; Blain et al. 1999). A submm survey for lenses (like ours) is not affected by this limitation. However, our models do not include the effect of shear, which has a well-known degeneracy with lens ellipticity (e.g., Keeton et al. 1997). We therefore view this as an interesting line of research for further study and urge caution when readers consider this result.

As a final note on the properties of the lensing galaxies discovered by *Herschel*, it is worth emphasizing the sample size at present and how large it might grow in the future. The SMA subsample consists of a subset of 30 candidate lensed SMGs selected from 104 objects with $S_{500} > 100$ mJy within ≈ 400 deg^2 of wide-field *Herschel* surveys. When the *Herschel* catalogs are complete, a total of ≈ 1000 deg^2 of sky will be surveyed and should provide a sample of ≈ 250 lens candidates. This is comparable to the expected number of lensed SMGs found by the full SPT survey (Vieira et al. 2013), but is already a factor of ≈ 5 larger than other source-selected or heterogeneous surveys such as CLASS or CASTLeS. It is also comparable in size to SLACS and the initial release of strong lenses from BELLS.

5. INTRINSIC PROPERTIES OF LENSED SMGs DISCOVERED BY *HERSCHEL*

In this section, we focus on the intrinsic properties of the SMA subsample of lensed SMGs. We begin by discussing the size bias inherent to samples of strongly lensed galaxies. We then compare our magnification measurements with statistical predictions. Next, we describe our methodology for measuring dust temperatures, intrinsic (i.e., unlensed) FIR luminosities and FIR luminosity surface densities for the SMA subsample by combining modified blackbody fitting of the SPIRE and SMA photometry with the magnification factors and intrinsic source sizes predicted by our lens models. Throughout, we define the L_{FIR} as integrated over 40–120 μm in the rest-frame (studies indicate a bolometric correction factor from L_{FIR} to L_{IR} of 1.91 is typical; e.g., Dale et al. 2001).

5.1. Size Bias in the SMA Subsample of Lensed SMGs

Strong gravitational lensing permits the study of SMGs at higher spatial resolutions than would otherwise be possible (e.g., a highly magnified SMG at $z = 2$ has been studied at 100 pc resolution with the SMA; Swinbank et al. 2010). While this is a highly attractive feature of strong lensing, it does necessitate certain unique considerations when transferring
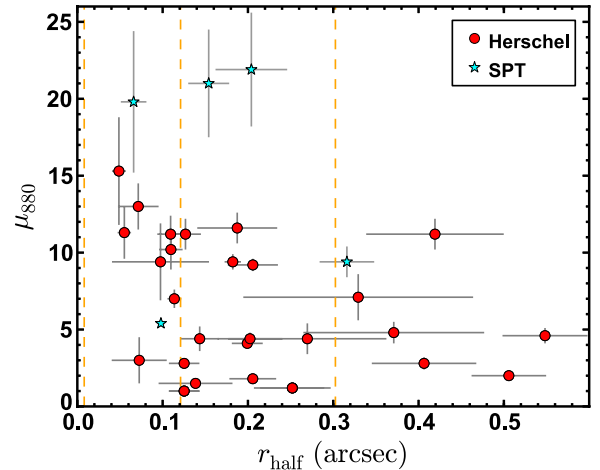
Figure 5. Magnification factor at 880 μm as a function of half-light radius for lensed SMGs discovered by *Herschel* (red circles) and SPT (cyan stars). The most highly magnified sources are also the smallest, consistent with expectations from theoretical models (Serjeant 2012; Hezaveh et al. 2012). Vertical dashed lines represent maximum achievable spatial resolution at 880 μm for unlensed sources with (from right to left) SMA, ALMA Cycle 1, and full ALMA. In some cases, strong lensing permits the SMA to resolve sources that would otherwise require baseline lengths of >10 km (i.e., full ALMA).

(A color version of this figure is available in the online journal.)

conclusions regarding lensed SMGs to the unlensed population. Chief amongst these considerations is the size bias inherent in any flux-limited sample of lensed galaxies. This bias has been investigated in a quantitative manner by a number of authors (Serjeant 2012; Hezaveh et al. 2012; Wardlow et al. 2013), who find that those objects with the brightest apparent flux densities should also have higher magnification factors and smaller sizes, on average.

Objects with high magnification factors are preferentially selected to have small sizes by flux-limited surveys like those of *Herschel* and SPT. This is because the degree of magnification depends primarily on the fraction of the source that is close to the caustic. A source that is extended relative to the size of the caustic will inevitably have a significant fraction of its flux density emitted in a region that is not highly magnified, so the total magnification factor summed over the entire source is not critically dependent on the exact location of the source relative to the caustic. Conversely, a population of lensed sources which are intrinsically compact will have a bimodal distribution of magnification factors that depends primarily on how far from the caustic the source is located. If a source is not highly magnified, it will likely not be bright enough to appear in our sample.

Figure 5 demonstrates this degeneracy between size (shown as half-light radius or r_{half}, where $r_{half} = a_s\sqrt{(1 - e_s)}$) and magnification factor (μ_{880}) for the SMA subsample and a handful of objects from SPT (Hezaveh et al. 2013). Our determinations of these values for the SMA subsample are presented in Table 6. Nearly every lensed SMG with $r_{half} < 0''.1$ is associated with $\mu_{880} > 10$. However, there are a surprising number of sources with $0''.1 < r_{half} < 0''.2$ and relatively modest magnification factors of $3 < \mu_{880} < 10$. We will return to the implications of the large number of low-magnification objects in Section 5.2.

For a source at $z = 2$, these sizes correspond to a physical scale of ≈ 1 kpc, which is at the low end of sizes measured for unlensed SMGs (Tacconi et al. 2006). It must be noted,

however, that there is a subtle bias when comparing the sizes of lensed and unlensed SMGs: if intrinsically low surface brightness regions are preferentially located farther from the caustic than high surface brightness regions (as expected for the reasons outlined above), then we expect the lensed SMGs to show smaller sizes than unlensed SMGs, because differential lensing makes detecting the low surface brightness regions more difficult than in the unlensed scenario.

Definitive measurements of the relative bias in the size measurements of lensed and unlensed SMGs will require spatially resolved observations of unlensed SMGs. The dashed vertical lines in Figure 5 illustrate both the advantages offered by lensing and the difficulties that must be overcome to assemble a statistically significant sample of unlensed SMGs with spatially resolved imaging. From right to left, the three lines indicate the maximum spatial resolutions available with the SMA, Cycle 1 ALMA, and full ALMA. It is only with the full ALMA and baselines > 10 km that spatial resolution better than $0\overset{''}{.}1$ can be achieved at these wavelengths—i.e., matching the best the SMA can do today for lensed SMGs discovered by *Herschel*.

5.2. Testing Predictions Derived from Lens Statistics

The number counts of unlensed SMGs fall off dramatically at the bright end of the luminosity function (e.g., Barger et al. 1999; Coppin et al. 2006; Oliver et al. 2010; Clements et al. 2010). This is the central reason why wide-field surveys at (sub-)mm wavelengths are useful tools for discovering strongly lensed galaxies (e.g., Blain 1996). There are several key elements of astrophysical interest in models which predict the magnification factor as a function of (sub-)mm flux density for strongly lensed galaxies found in wide-field (sub-)mm surveys. These are discussed in detail elsewhere (Perrotta et al. 2002; Negrello et al. 2007; Paciga et al. 2009; Hezaveh & Holder 2011; Wardlow et al. 2013), so we provide only the briefest of summaries here. In short, they are the lens mass profile (typically assumed to match the analytical form of Navarro–Frenk–White (NFW; Navarro et al. 1997) or a singular isothermal sphere) and the number densities of lenses and (unlensed) sources as functions of mass and redshift.

Figure 6 shows the magnification factor as a function of the 500 μm flux density for each strongly lensed SMG in the SMA subsample. Recall that we are complete for $S_{500} > 170$ mJy (see Section 2.1), except for one object which is the subject of a paper by H. Messias et al., (in preparation). The blue line is taken from Wardlow et al. (2013) and represents the predicted mean μ as a function of S_{500} for a complete sample of strongly lensed SMGs ($\mu > 2$). There are far more low-μ_{880} objects than expected based on the model. In fact, only two objects (J085358.9+015537 and J142825.5+345547) have μ_{880} values that are consistent at the 1σ level with the model predictions.

It is not presently clear why the model over-predicts the magnification factors at a given S_{500} value. One possibility is that our assumption of a single, smooth Sérsic profile for the background source leads to underestimates in some cases of the magnification factor. For example, one might imagine that a multi-component, clumpy model for the source morphology could reproduce the observed data while yielding larger magnification factors on average. Testing such models is beyond the scope of this paper, but we acknowledge that this possibility exists.

If the discrepancy between model and data is not simply a product of limited data quality, there still exist several possible explanations. Investigation into the dependence of the predicted
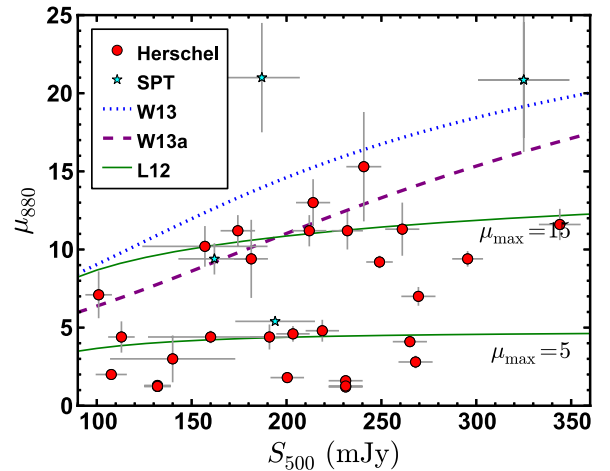
Figure 6. Magnification factor from the SMA lens model as a function of 500 μm flux density. The prediction for these values from Wardlow et al. (2013) is shown by the dotted blue line, whereas the dashed purple line traces the same model, but with parameters tuned to jointly match the observed number counts and magnification factors shown in this diagram. The solid green lines show the effects of different maximum magnifications and are taken from Lapi et al. (2012).

(A color version of this figure is available in the online journal.)

mean magnification on the various model parameters shows that this prediction is sensitive to a number of factors. The first of these is the shape of the intrinsic SMG number counts. The intrinsic counts are not well constrained at the bright end, primarily because of the contribution from lensed SMGs (Wardlow et al. 2013). Modest changes in the parameters of the Schechter function used to characterize the counts have a significant effect on the predicted mean magnification factor. This can be seen by a comparison of the dotted blue line in Figure 6, which traces the predicted $\mu_{880}(S_{500})$ curve from Wardlow et al. (2013) based on the observed number counts of SMGs, and the dashed purple line, which shows $\mu_{880}(S_{500})$ found from a satisfactory joint fit to the SMG number counts and the magnification measurements reported in Table 6. The Schechter function from the joint fit has a flatter slope (by 25%), a brighter characteristic flux density (by 15%), and a lower normalization (by 30%). It is also possible that a Schechter function provides an inadequate description of the bright end shape of the number counts (e.g., if blending is not properly taken into account; see Fu et al. 2013; Ivison et al. 2013; Hodge et al. 2013; Karim et al. 2013).

Another important parameter for predicting magnification factors is a fixed maximum magnification (μ_{max}), that is intended to reflect both the intrinsic sizes of the background sources as well as the typical angular separation between the centers of the sources and the centers of the lenses. The green lines shown in Figure 6 are taken from Lapi et al. (2012) and show the effect of this parameter on $\mu_{880}(S_{500})$. These curves help to highlight the apparent bimodality in μ_{880} values in the SMA subsample. One speculative explanation for this is a bimodal distribution of sizes in SMGs (this is supported by the sizes from the lens modeling; see Table 6 and Figure 5) and hence a bimodal distribution in μ_{max}. Larger samples and higher-spatial resolution are needed to confirm this intriguing possibility, which could plausibly result from SMGs comprising a population of rotating disks as well as major mergers. Such a study is beyond the scope of this paper and is therefore deferred to future publications.

Table 7
Intrinsic (i.e., Unlensed) Properties of SMA Sample (Assuming $\beta = 1.5$, Optically Thin Modified Blackbody, and L_{FIR} Integrated over 40–120 μm)

IAU Name	χ^2_{min}	T_{dust} (K)	$\log(M_{dust})$ ($M_\odot$)	$\log(L_{FIR})$ ($L_\odot$)	r_{half} (kpc)	$\log(\Sigma_{FIR})$ ($L_\odot$ kpc^{-2})
J021830.5−053124	7.11	36 ± 1	9.49 ± 0.11	12.79 ± 0.09	2.03 ± 0.71	11.45 ± 0.41
J022016.5−060143	4.46	37 ± 1	9.10 ± 0.10	12.79 ± 0.05	1.14 ± 0.37	11.93 ± 0.34
. . .	. . .	. . .	9.07 ± 0.10	12.76 ± 0.05	2.09 ± 0.35	11.34 ± 0.15
. . .	. . .	. . .	9.00 ± 0.10	12.67 ± 0.05	2.09 ± 0.39	11.24 ± 0.17
J083051.0+013224	0.86	44 ± 1	9.16 ± 0.06	13.09 ± 0.05	0.85 ± 0.07	12.44 ± 0.07
J084933.4+021443	9.62	36 ± 1	8.92 ± 0.05	12.72 ± 0.04	1.10 ± 0.22	11.86 ± 0.18
. . .	. . .	. . .	9.31 ± 0.05	13.11 ± 0.04	1.69 ± 0.19	11.87 ± 0.10
. . .	. . .	. . .	8.76 ± 0.05	12.56 ± 0.04	1.04 ± 0.42	11.85 ± 0.51
J085358.9+015537	0.98	36 ± 1	8.91 ± 0.09	12.37 ± 0.09	0.41 ± 0.08	12.37 ± 0.17
J090302.9−014127	1.13	38 ± 1	9.29 ± 0.07	12.92 ± 0.05	3.05 ± 0.92	11.20 ± 0.30
J090311.6+003906	0.87	34 ± 1	9.18 ± 0.06	12.45 ± 0.04	3.30 ± 0.65	10.63 ± 0.18
J090740.0−004200	10.30	43 ± 2	8.73 ± 0.10	12.58 ± 0.11	1.09 ± 0.62	11.92 ± 0.74
J091043.1−000321	25.66	41 ± 1	8.69 ± 0.06	12.50 ± 0.06	0.89 ± 0.16	11.82 ± 0.16
J091305.0−005343	0.04	35 ± 1	9.56 ± 0.08	12.94 ± 0.07	4.14 ± 0.72	10.92 ± 0.15
J105750.9+573026	2.64	47 ± 1	8.83 ± 0.05	12.94 ± 0.03	1.83 ± 0.26	11.62 ± 0.13
J114637.9−001132	1.86	41 ± 1	9.12 ± 0.06	12.90 ± 0.04	1.59 ± 0.13	11.70 ± 0.07
J125135.4+261457	2.24	39 ± 1	9.02 ± 0.06	12.68 ± 0.05	0.93 ± 0.21	11.97 ± 0.20
J125632.7+233625	0.41	40 ± 1	9.10 ± 0.07	12.80 ± 0.06	0.40 ± 0.07	12.80 ± 0.16
J132427.0+284452	47.59	37 ± 1	9.39 ± 0.07	12.92 ± 0.07	3.44 ± 0.44	11.05 ± 0.11
J132630.1+334410	13.33	36 ± 1	9.48 ± 0.04	13.00 ± 0.04	1.57 ± 0.17	11.81 ± 0.09
J133008.4+245900	1.14	43 ± 1	8.78 ± 0.06	12.66 ± 0.05	0.55 ± 0.24	12.52 ± 0.56
J133649.9+291801	7.62	39 ± 1	9.15 ± 0.09	12.87 ± 0.08	0.87 ± 0.34	12.27 ± 0.41
J134429.4+303036	6.90	38 ± 1	9.06 ± 0.04	12.73 ± 0.05	1.50 ± 0.40	11.62 ± 0.26
J141351.9−000026	23.28	38 ± 1	9.50 ± 0.08	13.18 ± 0.08	1.73 ± 0.31	11.92 ± 0.16
J142413.9+022303	0.49	41 ± 1	9.36 ± 0.05	13.17 ± 0.03	3.79 ± 0.38	11.22 ± 0.09
J142823.9+352619	6.14	39 ± 2	9.19 ± 0.20	12.77 ± 0.20	0.71 ± 0.43	12.52 ± 0.84
J142825.5+345547	0.88	38 ± 1	8.85 ± 0.10	12.45 ± 0.09	0.89 ± 0.18	11.77 ± 0.19
J143330.8+345439	0.84	39 ± 1	9.34 ± 0.06	12.96 ± 0.05	1.59 ± 0.34	11.78 ± 0.19

Note. Error bars are pertinent only to our chosen model and therefore underestimate the true uncertainties.

5.3. SED Fitting Methodology

All but two sources in this sample have short baseline SMA data (i.e., $D < 50$ m) that provide a robust total flux density at 880 μm. The exceptions are J132630.1+334410, which is resolved into two distinct images of the background source, and J142823.9+352619, which appears unresolved in extended array only data. We therefore expect that the SMA total flux density measurements are reliable for the entire sample. In conjunction with the *Herschel*/SPIRE photometry, these data can be used to measure the apparent (i.e., lensed) bolometric luminosity as well as the shape of the far-IR SED. In this section, we describe the methodology we use to undertake this task.

For galaxies at redshifts of $1.5 < z < 4.5$, *Herschel*/ SPIRE and SMA 880 μm photometry probe rest-frame 45 μm to 350 μm. At these wavelengths, the dominant contribution is thermal emission from dust heated by star-formation or an active galactic nucleus (AGN). We fit single-temperature, optically-thin, modified blackbody curves to the data, assuming an emissivity parameter of $\beta = 1.5$ (Hildebrand 1983). Studies based on *Infrared Astronomical Satellite* data have shown that this simple model gives a useful measure of the heating conditions of the ISM in galaxies (Desert et al. 1990). For the highest redshift sources ($z_{source} > 3.5$), the 250 μm channel of SPIRE probes the Wien side of the modified blackbody curve. The observed 250 μm flux density is under-predicted by this model if there are alternative powering sources that drive mid-IR luminosity (e.g., hot dust from AGN or intense SF). If such powering sources exist, the best-fit dust temperatures will be artificially inflated to compensate for the stronger 250 μm

emission. However, for the four objects in the SMA subsample at $z > 3.5$), we do not find evidence for significantly higher dust temperatures or poor fits to the data (see Table 7, indicating that a simple modified blackbody is a reasonable choice even for the high-redshift objects.

Another consideration that is important at high redshift is the influence of the cosmic microwave background (CMB) radiation. The CMB acts as an additional source of heating of the dust that shifts the SED to warmer temperatures and boosts the observed flux densities. However, for the dust temperatures and redshifts of the SMA subsample, this effect is insignificant (da Cunha et al. 2013) and we therefore do not incorporate it into our model fitting process.

The modified blackbody curve used here has the following form for the flux density, S_ν, given a dust temperature, T_{dust}:

$$S_\nu \propto \frac{\nu^{3+\beta}}{\exp(h\nu/kT_{dust}) - 1}. \quad (4)$$

An analysis of more complicated models that incorporate additional temperature components (e.g., Dunne & Eales 2001; Planck Collaboration et al. 2011) or allow the frequency at which the thermal emission becomes optically thick to vary (e.g., Hayward et al. 2012) is beyond the scope of this paper. This is because we are chiefly concerned with the apparent far-IR luminosities (μL_{FIR}) of the sources, which are relatively insensitive to the particular details of the chosen modified blackbody model. The dust temperature is also of interest here, but mainly for the purpose of comparison to existing samples of SMGs. Our choices here are well-matched to those that have

been made previously, thereby facilitating direct comparisons to the literature (e.g., Magnelli et al. 2012).

For a given μL_{FIR} and T_{dust}, we compute model flux densities at the *Herschel*/SPIRE and SMA bands by multiplying the modified blackbody curve with the appropriate filter function and integrating (for the SMA, we assume a top-hat filter shape with 8 GHz of bandwidth centered on ν_{LO}). Calibration uncertainties are accounted for by adding 7% uncertainty in quadrature to each photometric measurement. Confusion noise is also included, though it is largely insignificant at the flux densities of the lensed SMGs. We use the EMCEE software package to iterate over plausible ranges in μL_{FIR} (10^{10}–$10^{15}\ L_\odot$) and T_{dust} (20–100 K) values for each lensed SMG (see Section 3.1 for a description of the behavior of EMCEE). We use 100 walkers and 200 iterations in the "burn-in" stage to converge on the best-fit model, keeping in mind the additional 7% absolute flux density calibration uncertainty in the *Herschel*/SPIRE and SMA photometry. In the final stage, we use 100 walkers and 10 iterations for a total of 1000 sets of model parameters. These provide the shape of the posterior probability density functions for μL_{FIR} and T_{dust}, which are then used to compute the best-fit values and the 1σ confidence intervals. We use our measurements of μ_{880} from Section 5 to obtain the intrinsic, unlensed FIR luminosity, L_{FIR}. Finally, we compute dust masses using the standard equation (Hildebrand 1983),

$$M_{dust} = \frac{1}{1 + z_s} \frac{S_{880} d_L^2}{\kappa_d^{rest} B(\nu^{rest}, T_{dust})}, \qquad (5)$$

where κ_d^{rest} is the mass absorption coefficient and $B(\nu^{rest}, T_{dust})$ is the value of the blackbody function for the given T_{dust} and computed at the rest-frame frequency ν^{rest}. We obtain κ_d^{rest} by interpolation of the values in Draine (2003) over the appropriate range in rest-frame wavelength. The uncertainty in κ_d^{rest} is a factor of a few and dominates the total error budget for our dust mass estimates.

We follow the procedure outlined here for all SMGs with *Herschel*/SPIRE and submm photometry. Besides the objects in this paper, this also includes SMGs from Hezaveh et al. (2013) (with photometry and redshifts coming from Weiß et al. 2013; Bothwell et al. 2013) and Magnelli et al. (2012).

5.4. The SEDs of Herschel-selected Lensed SMGs

The results of our SED fitting procedure are given for the SMA subsample in Table 7, including the best-fit reduced chi-squared value (χ_{min}^2), the dust temperature (T_{dust}), the dust mass (M_{dust}; error bars do not include the factor of a few uncertainty in the mass opacity coefficient), the FIR luminosity (L_{FIR}), the half-light radius (r_{half}), and the FIR luminosity surface density (Σ_{FIR}). The error bars are pertinent only to our chosen model of a single optically thin modified blackbody. In this table, the magnification factor and uncertainty inferred from the lens model have been used to compute intrinsic values and their uncertainties. For 13 objects, $\chi_{min}^2 > 2$, suggesting that the single-component modified blackbody model is an over-simplification in nearly half of the SMA subsample.

The T_{dust}–L_{FIR} diagram is useful for characterizing the shape and amplitude of the rest-frame far-IR SED of dusty galaxies. Figure 7 shows these parameters for the objects in the SMA subsample, a handful of SPT lensed SMGs (Hezaveh et al. 2013), and a sample of primarily unlensed SMGs (Magnelli et al. 2012). Some of the objects in this diagram are known to have multiple components in the source plane (e.g., J022016.5−060143). In
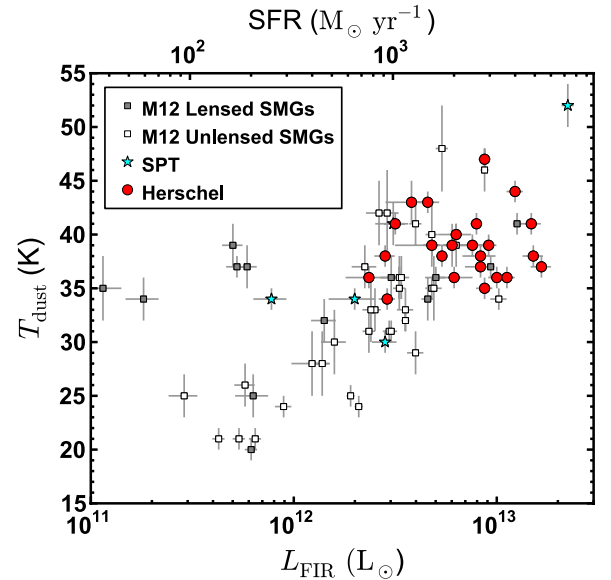
Figure 7. Dust temperature as a function of intrinsic (i.e., unlensed) FIR luminosity for lensed SMGs discovered by *Herschel* (red circles) and SPT (cyan stars), as well as unlensed and lensed SMGs from Magnelli et al. (2012; gray squares). Error bars include uncertainty in magnification factors.

(A color version of this figure is available in the online journal.)

these cases, we show the L_{FIR} value integrated over all components in the source plane. This is primarily done because our measurements of T_{dust} are based on *Herschel* photometry in large part, which does not resolve the individual components in the source plane.

Objects in the SMA subsample populate the high-L_{FIR}, high-T_{dust} regime (median $L_{FIR} = 7.9 \times 10^{12}\ L_\odot$, median $T_{dust} = 39$ K) compared to unlensed SMGs (median $L_{FIR} = 2.8 \times 10^{12}\ L_\odot$, median $T_{dust} = 32$ K). The selection of the brightest objects found in wide-field surveys is the dominant reason for the high L_{FIR} values reported here. However, thanks to lensing, we probe a relatively wide range in L_{FIR}: 2.7–17.0 $\times 10^{12}\ L_\odot$, despite selecting the brightest objects at 500 μm. The top axis in Figure 7 shows the star formation rates (SFRs) that are inferred based on the Kennicutt (1998) prescription for converting L_{IR} (computed from L_{FIR} assuming a bolometric correction factor of 1.91; Dale et al. 2001) to SFR assuming a Salpeter IMF. Finally, the high dust temperatures in the SMA subsample reflect the fact that a greater portion of the IR luminosity is emitted at short wavelengths in the highest luminosity sources. This result is consistent with what has been found previously for lensed SMGs (Harris et al. 2012) as well as for unlensed SMGs (Magnelli et al. 2012) and is one of the first indications that *Herschel*-selected lensed SMGs are not greatly dissimilar in their physical properties from unlensed SMGs (the same conclusion is reached by Harris et al. 2012).

5.5. Size Scale of Star-formation in Herschel-selected Lensed SMGs

One of the central themes in understanding the evolution of the most luminous galaxies during the epoch of peak SFR density in the universe (i.e., $1 < z < 4$; e.g., Burgarella et al. 2013) is the role played by major mergers. It has been clear for decades that the most luminous galaxies at $z \sim 0$—commonly known as ultra-luminous infrared galaxies (ULIRGs) and defined to have $L_{IR} > 10^{12}\ L_\odot$— are powered by major mergers (e.g., Armus et al. 1987; Clements et al. 1996;
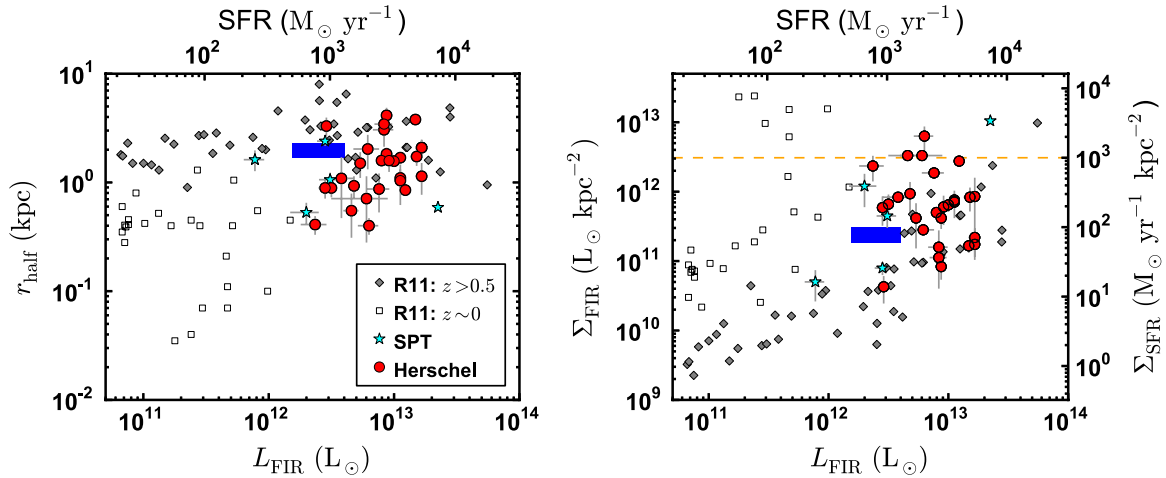
Figure 8. Left: half-light radius as a function of FIR luminosity for lensed SMGs discovered by *Herschel* (red circles) and SPT (cyan stars), as well as galaxies from a compilation in Rujopakarn et al. (2011) at $z > 0.5$ (filled gray diamonds) and at $z \sim 0$ (open squares). The blue shaded region represents the median and 1σ range found for unlensed SMGs by Tacconi et al. (2006). Right: far-IR luminosity surface density as a function of FIR luminosity. The orange dashed line traces the theoretical limit of Σ_{SFR} for an optically thick disk (Thompson et al. 2005). The SMA subsample spans nearly one decade in L_{FIR} and two decades in Σ_{FIR}. A handful of sources approach or exceed the highest values observed in local LIRGs and ULIRGs ($\Sigma_{FIR} = 10^{13} L_\odot$ kpc^{-2}).

(A color version of this figure is available in the online journal.)

Murphy et al. 1996). However, it is also clear that such systems contribute only trivially to the SFR density in the universe today because they are so rare (Soifer et al. 1986). Since ULIRGs contribute an increasing fraction of the total SFR density as a function of redshift (e.g., Le Floc'h et al. 2005; Magnelli et al. 2011), some theoretical efforts have suggested that an increase in the merger rate in conjunction with strong inflows of gas from the intergalactic medium (IGM) at high redshift could allow the merger paradigm to explain a large fraction of the luminous galaxies at these epochs (e.g., Hopkins et al. 2010). Providing support for this theoretical paradigm are sub-arcsecond observations of CO emission in a handful of SMGs which show that a significant fraction of SMGs that are spatially resolved have multiple, similar mass components—i.e., they are major mergers (Tacconi et al. 2008; Engel et al. 2010; Ivison et al. 2011; Riechers et al. 2011a).

On the other hand, some recent theoretical attempts to simulate the formation of galaxies on cosmological scales (i.e., cubes that are ≈ 200 Mpc on a side) have found evidence that favors a model of galaxy formation in which smooth flows of gas from the IGM feed large, extended reservoirs of gas in disk galaxies (e.g., Kereš et al. 2009; Davé et al. 2010). There is even observational evidence based on dynamical models that disk-like systems exist at high redshift (Hodge et al. 2012). Ultimately, detailed dynamical models of statistically significant samples can resolve the dispute between the merger and disk paradigms. However, assembling the requisite datasets is extremely expensive in terms of telescope time. A far more feasible goal is spatially resolved observations of the dust emission in SMGs at high redshift.

The dust emission in SMGs is critically important because it represents reprocessed emission from young massive stars which provide a reliable measure of the instantaneous SFR (within the past ≈ 10 Myr). This assumes no significant contribution from a cold, diffuse ISM component (supported by our measurements of T_{dust}) and no significant contribution from an AGN (our use of the FIR luminosity integrated over 40–120 μm rest-frame is intended to mitigate this possibility). Measuring the size-scale and the luminosity of this dust can therefore in principle be used to contrast extended galaxy morphologies ex-

pected from accretion-fuelled disks (e.g., Dekel et al. 2009) and compact morphologies expected from dissipational mergers of gas-rich disks (e.g., Mihos & Hernquist 1996).

The left panel of Figure 8 shows the physical sizes (circularized radii, r_{half}) as a function of L_{FIR} for the SMA subsample and the SPT sample (Hezaveh et al. 2013). In this figure, objects with multiple components in the source plane are plotted individually, unlike in Figure 7. In doing this, we have assumed that the FIR luminosity in each component is proportional to its intrinsic flux density at 880 μm from the lens model (i.e., $\mu_{FIR} \approx \mu_{880}$). This assumption is consistent with our modeling efforts because the only time we use multiple components in the source plane is when it is clear that only moderate lensing is occurring, in which case $\mu_{FIR} \approx \mu_{880}$ is a valid approximation. Two comparison samples of unlensed LIRGs and ULIRGs from Rujopakarn et al. (2011) are shown: one at $0.5 < z < 2.5$ and one at $z \sim 0$. The sample of intermediate and high redshift LIRGs and ULIRGs relies on size measurements based primarily on radio observations (Chapman et al. 2004; Muxlow et al. 2005; Biggs & Ivison 2008; Casey et al. 2009), but also includes a handful of with mm size measurements (Tacconi et al. 2006, 2010; Daddi et al. 2010) and the assumption that the radio and far-IR sizes are correlated. Finally, Figure 8 also shows the median and 1σ range in these values for a handful of unlensed SMGs with high-spatial resolution imaging by Tacconi et al. (blue rectangle; 2006).

We find a wide range in sizes for the SMA subsample: the minimum, median, and maximum r_{half} values are 0.41 kpc, 1.53 kpc, and 4.16 kpc. In comparison, Rujopakarn et al. (2011) find values of 0.9 kpc, 2.6 kpc, and 8.0 kpc for the intermediate and high redshift sample. Part of this difference is a result of lensing, which lets us access spatial resolutions that are otherwise inaccessible (the radio observations used to measure sizes in the comparison sample have a typical angular resolution of 0″.15, corresponding to a physical scale of ≈ 1 kpc at the redshifts of interest). Local LIRGs and ULIRGs have smaller sizes than their higher redshift counterparts (Rujopakarn et al. 2011), but the sizes of objects in the SMA subsample begin to overlap with those of the local LIRGs and ULIRGs. Very strong lensing (e.g., $\mu \gtrsim 30$) can reach ≈ 100 pc scale spatial
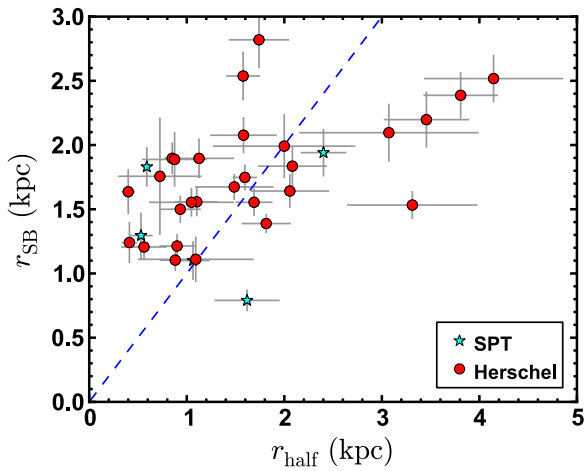
Figure 9. Comparison of size measurements (r_{SB}) computed from application of Stefan–Boltzmann law to intrinsic IR luminosities and dust temperatures with those obtained from direct measurements from lens models (circularized half-light radius, r_{half}). A dashed blue line traces $r_{SB} = r_{half}$. Approximately 75% of the sample has $r_{half} \lesssim r_{SB}$. For these sources, the FIR emission is likely to be optically thick.

(A color version of this figure is available in the online journal.)

resolution (Swinbank et al. 2010), but these occurrences must be rare because no such object is found in the SMA subsample.

The right panel of Figure 8 shows the FIR luminosity surface density (Σ_{FIR}) as a function of L_{FIR} for the same set of objects as in the left panel. A wide range in Σ_{FIR} is evident for the SMA subsample: the minimum, median, and maximum Σ_{FIR} values are 0.05, 0.6, and 6.0×10^{12} $L_\odot$ kpc^{-2}, respectively. A horizontal line drawn at 1000 $M_\odot$ yr^{-1} kpc^{-2} represents the theoretical limit for SFR surface density in a sustainable radiation-pressure supported disk (Thompson et al. 2005). A handful of objects in the SMA subsample and one object in the SPT sample lie near to or in excess of this limit, possibly indicating that they are in a very short-lived phase of evolution (e.g., the coalescence stage of a major merger). There are also, however, a number of objects with Σ_{FIR} values more than an order of magnitude below the limit, suggesting that multiple modes of star-formation are viable in high redshift SMGs.

A spherically symmetric dust source radiating as a blackbody obeys the Stefan–Boltzmann law relating emitted flux density and the temperature of the dust. We use this fact to infer an alternative measure of the size of the lensed SMG, which we denote as r_{SB}:

$$r_{SB} = \sqrt{\frac{L_{IR}}{4\pi\,\sigma_{SB} T_{dust}^4}} \qquad (6)$$

where σ_{SB} is the Stefan–Boltzmann constant. This quantity is similar in scope to the "effective radius" described in Greve et al. (2012) for lensed SMGs discovered by the SPT. Figure 9 shows the results of this analysis for the SMA and SPT samples. In this diagram, the error bars reflect the formal values obtained for our given set of model assumptions—e.g., the uncertainty introduced by the assumption of a single-temperature modified blackbody is not included. A dashed line traces the 1:1 relation between these two measures of the size (i.e., $r_{SB} = r_{half}$).

A total of 15 out of 23 sources satisfy the unphysical criterion of $r_{SB} > r_{half}$. The best explanation for the large number of sources that violate the blackbody limit is that our T_{dust} values are underestimated by the assumption of optically thin emission. In fact, $r_{SB} \approx r_{half}$ suggests optically thick FIR emission.

Adopting an optically thick model for the SED fitting would lead to larger dust temperatures by 25%–50%, an increase that is nearly sufficient for all of the sources in our sample to satisfy $r_{SB} < r_{half}$. The exact geometry of the source is unknown and is therefore an additional complicating factor. Nevertheless, this crude line of analysis is one indication that the FIR emission is optically thick in lensed SMGs discovered by *Herschel*, similar to local ULIRGs, which have $r_{half} \approx 2–3 \times r_{SB}$ (Solomon et al. 1997). Only a handful of sources have large r_{half} values and low Σ_{FIR} values typical of optically thin disks far from the Eddington limit (e.g., J091305.0−005343).

6. CONCLUSIONS

We present sub-arcsecond submm imaging from the SMA for 30 strong lens candidates discovered by *Herschel* in the H-ATLAS and HerMES wide-field surveys. The candidates are selected to have $S_{500} > 100$ mJy and the SMA subsample contains nearly all targets with $S_{500} > 170$ mJy. We also present optical spectroscopy from the MMT, Gemini-S, and WHT that provide new redshift measurements for 8 of the putative lenses. Nearly all candidates in the SMA subsample have existing spectroscopic redshifts for the putative lensed SMGs from blind CO searches with the GBT (Harris et al. 2012), CSO (Lupu et al. 2012), CARMA (D. A. Riechers et al., in preparation), and PdBI (Cox et al. 2011; M. Krips et al., in preparation).

Out of the SMA subsample of 30, there are 16 that have distinct lens and source redshifts and obvious lensed morphology in the submm ("grade A" lenses). Four objects have convincing morphological signatures of lensing, but only one spectroscopic redshift measurement—we consider these to be highly likely to be strongly lensed ("grade B" lenses). Another five objects have distinct redshift measurements for lens and source, but the SMA imaging reveals only one image of the background source, suggesting modest magnification factors: $\mu_{880} < 2$ ("grade C" lenses). Finally, there are five objects that lack distinct redshift measurements and do not show obvious morphological signatures of lensing—additional data are needed to determine whether or not these "grade X" systems are strongly lensed. In total, the strong lensing rate is 70%–87% (83%–100% if moderately lensed systems are included as well).

We use the SMA data to develop lens models in the visibility plane, as is appropriate for interferometers like the SMA. We derive lens models for the 25 objects with obvious signatures of lensing (either strong or moderate) in the submm. In conjunction with redshifts from optical and mm-wave spectroscopy, the lens models provide measurements of the mass of the lenses inside the Einstein radius, as well as the size and far-IR luminosity of the lensed SMGs.

We find that the lenses are at higher redshifts and have lower masses than lenses found in surveys based on SDSS optical spectroscopy, in agreement with expectations for a source-selected (rather than lens-selected) survey for lenses. The number of lenses that will be found from wide-field (sub-)mm surveys (González-Nuevo et al. 2012) promises to be comparable to that from SDSS-based searches, but the former provide access to a population of lenses with fundamentally different properties. For this reason, lenses found by *Herschel* and SPT are highly complementary to those found by SDSS and will remain so for the foreseeable future.

The lensed SMGs probe over a decade in sizes (median circularized half-light radii of 1.6 kpc) and intrinsic (i.e., unlensed) FIR luminosity (median L_{FIR} of 7.9×10^{12} $L_\odot$). Applying the Kennicutt (1998) prescription to convert L_{IR}

to SFR, we use the sizes and $L_{\rm FIR}$ values to infer a nearly two-decade range in SFR surface density (median $\Sigma_{\rm SFR} = 200\ M_\odot\ {\rm yr}^{-1}\ {\rm kpc}^{-2}$). A handful of lensed SMGs lie near or above the theoretical limit of $\Sigma_{\rm SFR} = 1000\ M_\odot\ {\rm yr}^{-1}\ {\rm kpc}^{-2}$ for an optically thick disk, but there are also several objects with $\Sigma_{\rm SFR}$ values over an order of magnitude below this limit, implying that multiple modes of star-formation may be required to explain SMGs at $z \gtrsim 1.5$.

The magnification factors we measure for the lensed SMGs are significantly lower than predicted from models based on number counts of unlensed SMGs. This may be an indication that the bright end of the SMG luminosity function or the intrinsic sizes of SMGs are currently poorly understood.

Finally, it is worth emphasizing that the advent of ALMA makes the future in this field looks very promising. Many of the unsolved questions from this work can be addressed in a direct manner by obtaining more sensitive submm observations at higher spatial resolution. For a given amount of integration time, ALMA (when fully operational) will provide factors of 10–100 improvement in these quantities compared to the SMA.

Facilities: SMA, MMT, Gemini:South, ING:Herschel, VLT:Melipal

REFERENCES

Armus, L., Heckman, T., & Miley, G. 1987, AJ, 94, 831
Barger, A. J., Cowie, L. L., Smail, I., et al. 1999, AJ, 117, 2656
Bartelmann, M., & Loeb, A. 1998, ApJ, 503, 48
Becker, R. H., White, R. L., & Helfand, D. J. 1995, ApJ, 450, 559
Benn, C., Dee, K., & Agócs, T. 2008, Proc., SPIE, 7014
Biggs, A. D., & Ivison, R. J. 2008, MNRAS, 385, 893
Blain, A. W. 1996, MNRAS, 283, 1340
Blain, A. W., & Longair, M. S. 1993, MNRAS, 264, 509
Blain, A. W., Moller, O., & Maller, A. H. 1999, MNRAS, 303, 423
Bolton, A. S., Burles, S., Koopmans, L. V. E., et al. 2008, ApJ, 682, 964
Borys, C., Blain, A. W., Dey, A., et al. 2006, ApJ, 636, 134
Bothwell, M. S., Aguirre, J. E., Chapman, S. C., et al. 2013, in press (arXiv:1309.3275)
Brewer, B. J., Dutton, A. A., Treu, T., et al. 2012, MNRAS, 422, 3574
Browne, I. W. A., Wilkinson, P. N., Jackson, N. J. F., et al. 2003, MNRAS, 341, 13
Brownstein, J. R., Bolton, A. S., Schlegel, D. J., et al. 2012, ApJ, 744, 41
Bruzual, G., & Charlot, S. 2003, MNRAS, 344, 1000
Burgarella, D., Buat, V., Gruppioni, C., et al. 2013, A&A, 554, A70
Bussmann, R. S., Gurwell, M. A., Fu, H., et al. 2012, ApJ, 756, 134
Carlstrom, J. E., Ade, P. A. R., Aird, K. A., et al. 2011, PASP, 123, 568
Casey, C. M., Chapman, S. C., Beswick, R. J., et al. 2009, MNRAS, 399, 121
Chapman, S. C., Smail, I., Windhorst, R., Muxlow, T., & Ivison, R. J. 2004, ApJ, 611, 732
Clements, D. L., Rigby, E., Maddox, S., et al. 2010, A&A, 518, L8
Clements, D. L., Sutherland, W. J., McMahon, R. G., & Saunders, W. 1996, MNRAS, 279, 477
Condon, J. J., Cotton, W. D., Greisen, E. W., et al. 1998, AJ, 115, 1693
Conley, A., Cooray, A., Vieira, J. D., et al. 2011, ApJL, 732, L35
Coppin, K. E. K., Chapin, E. L., Mortier, A. M. J., et al. 2006, MNRAS, 372, 1621

Cox, P., Krips, M., Neri, R., et al. 2011, ApJ, 740, 63
da Cunha, E., Groves, B., Walter, F., et al. 2013, ApJ, 766, 13
Daddi, E., Bournaud, F., Walter, F., et al. 2010, ApJ, 713, 686
Dale, D. A., Helou, G., Contursi, A., Silbermann, N. A., & Kolhatkar, S. 2001, ApJ, 549, 215
Davé, R., Finlator, K., Oppenheimer, B. D., et al. 2010, MNRAS, 404, 1355
de Zotti, G., Ricci, R., Mesa, D., et al. 2005, A&A, 431, 893
Dekel, A., Sari, R., & Ceverino, D. 2009, ApJ, 703, 785
Desert, F.-X., Boulanger, F., & Puget, J. L. 1990, A&A, 237, 215
Diolaiti, E., Bendinelli, O., Bonaccini, D., et al. 2000, Proc. SPIE, 4007, 879
Draine, B. T. 2003, ARA&A, 41, 241
Dunne, L., & Eales, S. A. 2001, MNRAS, 327, 697
Eales, S., Dunne, L., Clements, D., et al. 2010, PASP, 122, 499
Eisenstein, D. J., Weinberg, D. H., Agol, E., et al. 2011, AJ, 142, 72
Engel, H., Tacconi, L. J., Davies, R. I., et al. 2010, ApJ, 724, 233
Foreman-Mackey, D., Hogg, D. W., Lang, D., & Goodman, J. 2013, PASP, 125, 306
Frayer, D. T., Harris, A. I., Baker, A. J., et al. 2011, ApJL, 726, L22
Fu, H., Cooray, A., Feruglio, C., et al. 2013, Natur, 498, 338
Fu, H., Jullo, E., Cooray, A., et al. 2012, ApJ, 753, 134
Gavazzi, R., Cooray, A., Conley, A., et al. 2011, ApJ, 738, 125
George, R. D., Ivison, R. J., Hopwood, R., et al. 2013, MNRAS, 436, L104
Gladders, M. D., & Yee, H. K. C. 2005, ApJS, 157, 1
Goldoni, P., Royer, F., François, P., et al. 2006, Proc. SPIE, 6269, 62692K
González-Nuevo, J., Lapi, A., Fleuren, S., et al. 2012, ApJ, 749, 65
Goodman, J., & Weare, J. 2010, Comm. Appl. Math. Comput. Sci., 5, 65
Greve, T. R., Vieira, J. D., Weiß, A., et al. 2012, ApJ, 756, 101
Griffin, M. J., Abergel, A., Abreu, A., et al. 2010, A&A, 518, L3
Harris, A. I., Baker, A. J., Frayer, D. T., et al. 2012, ApJ, 752, 152
Hayward, C. C., Jonsson, P., Kereš, D., et al. 2012, MNRAS, 424, 951
Hezaveh, Y. D., & Holder, G. P. 2011, ApJ, 734, 52
Hezaveh, Y. D., Marrone, D. P., Fassnacht, C. D., et al. 2013, ApJ, 767, 132
Hezaveh, Y. D., Marrone, D. P., & Holder, G. P. 2012, ApJ, 761, 20
Hildebrand, R. H. 1983, QJRAS, 24, 267
Ho, P. T. P., Moran, J. M., & Lo, K. Y. 2004, ApJL, 616, L1
Hodge, J. A., Carilli, C. L., Walter, F., et al. 2012, ApJ, 760, 11
Hodge, J. A., Karim, A., Smail, I., et al. 2013, ApJ, 768, 91
Hook, I. M., Jørgensen, I., Allington-Smith, J. R., et al. 2004, PASP, 116, 425
Hopkins, P. F., Younger, J. D., Hayward, C. C., Narayanan, D., & Hernquist, L. 2010, MNRAS, 402, 1693
Ikarashi, S., Kohno, K., Aguirre, J. E., et al. 2011, MNRAS, 415, 3081
Inada, N., Oguri, M., Shin, M.-S., et al. 2012, AJ, 143, 119
Ivison, R. J., Papadopoulos, P. P., Smail, I., et al. 2011, MNRAS, 412, 1913
Ivison, R. J., Swinbank, A. M., Smail, I., et al. 2013, ApJ, 772, 137
Karim, A., Swinbank, A. M., Hodge, J. A., et al. 2013, MNRAS, 432, 2
Keeton, C. R. 2001, arXiv:astro-ph/0102340
Keeton, C. R., Kochanek, C. S., & Seljak, U. 1997, ApJ, 482, 604
Kennicutt, R. C., Jr. 1998, ARA&A, 36, 189
Kereš, D., Katz, N., Fardal, M., Davé, R., & Weinberg, D. H. 2009, MNRAS, 395, 160
King, L. J., & Browne, I. W. A. 1996, MNRAS, 282, 67
Kreysa, E., Gemuend, H.-P., Gromke, J., et al. 1998, Proc. SPIE, 3357, 319
Lapi, A., Negrello, M., González-Nuevo, J., et al. 2012, ApJ, 755, 46
Le Floc'h, E., Papovich, C., Dole, H., et al. 2005, ApJ, 632, 169
Lupu, R. E., Scott, K. S., Aguirre, J. E., et al. 2012, ApJ, 757, 135
Magnelli, B., Elbaz, D., Chary, R. R., et al. 2011, A&A, 528, A35
Magnelli, B., Lutz, D., Santini, P., et al. 2012, A&A, 539, A155
Marsden, D., Gralla, M., Marriage, T. A., et al. 2013, arXiv:1306.2288

Mihos, J. C., & Hernquist, L. 1996, ApJ, 464, 641
Mocanu, L. M., Crawford, T. M., Vieira, J. D., et al. 2013, arXiv:1306.3470
Muñoz, J. A., Falco, E. E., Kochanek, C. S., et al. 1998, Ap&SS, 263, 51
Murphy, T. W., Jr., Armus, L., Matthews, K., et al. 1996, AJ, 111, 1025
Muxlow, T. W. B., Richards, A. M. S., Garrington, S. T., et al. 2005, MNRAS, 358, 1159
Myers, S. T., Jackson, N. J., Browne, I. W. A., et al. 2003, MNRAS, 341, 1
Navarro, J. F., Frenk, C. S., & White, S. D. M. 1997, ApJ, 490, 493
Negrello, M., Hopwood, R., De Zotti, G., et al. 2010, Sci, 330, 800
Negrello, M., Perrotta, F., González-Nuevo, J., et al. 2007, MNRAS, 377, 1557
Nguyen, H. T., Schulz, B., Levenson, L., et al. 2010, A&A, 518, L5
Oliver, S. J., Bock, J., Altieri, B., et al. 2012, MNRAS, 424, 1614
Oliver, S. J., Wang, L., Smith, A. J., et al. 2010, A&A, 518, L21
Omont, A., Neri, R., Cox, P., et al. 2011, A&A, 530, L3
Paciga, G., Scott, D., & Chapin, E. L. 2009, MNRAS, 395, 1153
Pascale, E., Auld, R., Dariush, A., et al. 2011, MNRAS, 415, 911
Perrotta, F., Baccigalupi, C., Bartelmann, M., De Zotti, G., & Granato, G. L. 2002, MNRAS, 329, 445
Pilbratt, G. L., Riedinger, J. R., Passvogel, T., et al. 2010, A&A, 518, L1
Planck Collaboration, Ade, P. A. R., Aghanim, N., et al. 2011, A&A, 536, A16
Riechers, D. A., Carilli, L. C., Walter, F., et al. 2011a, ApJL, 733, L11
Riechers, D. A., Cooray, A., Omont, A., et al. 2011b, ApJL, 733, L12
Rigby, E. E., Maddox, S. J., Dunne, L., et al. 2011, MNRAS, 415, 2336
Roseboom, I. G., Oliver, S. J., Kunz, M., et al. 2010, MNRAS, 409, 48
Rujopakarn, W., Rieke, G. H., Eisenstein, D. J., & Juneau, S. 2011, ApJ, 726, 93
Sault, R. J., Teuben, P. J., & Wright, M. C. H. 1995, in ASP Conf. Ser. 77, Astronomical Data Analysis Software and Systems IV, ed. R. A. Shaw, H. E. Payne, & J. J. E. Hayes (San Francisco, CA: ASP), 433
Schmidt, G. D., Weymann, R. J., & Foltz, C. B. 1989, PASP, 101, 713
Schneider, P., Ehlers, J., & Falco, E. E. 1992, Gravitational Lenses (Berlin: Springer)
Schneider, P., Kochanek, C. S., & Wambsganss, J. 2006, Gravitational Lensing: Strong, Weak and Micro: Saas-Fee Advanced Courses 33 (Berlin: Springer)
Scott, K. S., Lupu, R. E., Aguirre, J. E., et al. 2011, ApJ, 733, 29
Serjeant, S. 2012, MNRAS, 424, 2429
Serjeant, S., & Harrison, D. 2005, MNRAS, 356, 192
Sersic, J. L. 1968, Atlas de Galaxias Australes (Cordoba, Argentina: Observatorio Astronomico)
Soifer, B. T., Sanders, D. B., Neugebauer, G., et al. 1986, ApJL, 303, L41
Solomon, P. M., Downes, D., Radford, S. J. E., & Barrett, J. W. 1997, ApJ, 478, 144
Sonnenfeld, A., Gavazzi, R., Suyu, S. H., Treu, T., & Marshall, P. J. 2013, arXiv:1307.4764
Swetz, D. S., Ade, P. A. R., Amiri, M., et al. 2011, ApJS, 194, 41
Swinbank, A. M., Smail, I., Longmore, S., et al. 2010, Natur, 464, 733
Tacconi, L. J., Genzel, R., Neri, R., et al. 2010, Natur, 463, 781
Tacconi, L. J., Genzel, R., Smail, I., et al. 2008, ApJ, 680, 246
Tacconi, L. J., Neri, R., Chapman, S. C., et al. 2006, ApJ, 640, 228
Thompson, T. A., Quataert, E., & Murray, N. 2005, ApJ, 630, 167
Treu, T. 2010, ARA&A, 48, 87
Vernet, J., Dekker, H., D'Odorico, S., et al. 2011, A&A, 536, A105
Vieira, J. D., Crawford, T. M., Switzer, E. R., et al. 2010, ApJ, 719, 763
Vieira, J. D., Marrone, D. P., Chapman, S. C., et al. 2013, Natur, 495, 344
Wardlow, J. L., Cooray, A., De Bernardis, F., et al. 2013, ApJ, 762, 59
Weiß, A., De Breuck, C., Marrone, D. P., et al. 2013, ApJ, 767, 88